Universidad de Valladolid

UNIVERSIDAD DE VALLADOLID

ESCUELA DE INGENIERIAS INDUSTRIALES

Máster en Ingeniería Química

Bismuth vanadate, bismuth oxyiodide and bismuth oxybromide thin films growth via Aerosol-Assisted CVD as the main process and their photoelectrochemical properties

Autor:
Vicente Matas, Javier

Mato Chaín, Rafael Bartolome

Imperial College London

Londres, Enero 2022.

TFM REALIZADO EN PROGRAMA DE INTERCAMBIO

TÍTULO:	Bismuth vanadate, bismuth oxyiodide and bismuth oxybromide thin films growth via Aerosol-Assisted CVD as the main process and their photoelectrochemical properties
ALUMNO:	Javier Vicente Matas
FECHA:	07 de Enero de 2021
CENTRO:	Faculty of Engineering, South Kensington Campus
UNIVERSIDAD:	Imperial College London
TUTOR:	Dr. Salvador Eslava

Content

RESUMEN Y PALABRAS CLAVE

Este trabajo propone la síntesis de fotoelectrodos de vanadato de bismuto ($BiVO_4$), óxido de bromuro de bismuto (BiOBr) y óxido de yoduro de bismuto (BiOI) en sustratos de flúor dopado de vidrio de óxido de estaño (FTO) a trasvés de un proceso AACVD de una etapa o un proceso AACVD de dos etapas para su utilización en PEC devices. Los fotoelectrodos se caracterizan por difracción de rayos X (XRD), Raman espectroscopía (RS), espectroscopía UV-VIS y Microscopia electrónica de rastreo (SEM). Las propiedades fotoelectroquímicas (PEC) de los fotoelectrodos se estudiaron en Na_2SO_4 acuoso 0.5 M y muestran que el mejor valor fue el BiOI depositado durante 5 horas y 350 ºC (1,1 mA cm^{-2} a 1,23 V vs RHE). Aunque el objetivo inicial era obtener $BiVO_4$, tanto en el proceso de dos pasos como en el de un paso se obtuvieron valores inferiores con respecto a la deposición de BiOI. En el proceso de dos pasos, el mejor valor fue la deposición para 5h y 350 ºC (0.7 mA cm^{-2} a 1.23V vs RHE). En el proceso de un solo paso, la mala adhesión con el FTO produjo valores bajos.

Palabras clave: AACVD, $BiVO_4$ BiOI BiOBr, División de agua fotoelectroquímica, Fotoelectrodo, Dispositivos PEC.

ABSTRACT AND KEYWORDS

This work proposes the synthesis of photoelectrodes of bismuth vanadate ($BiVO_4$), bismuth bromide oxide (BiOBr), and bismuth iodide oxide (BiOI) on tin oxide glass doped fluorine substrates (FTO) through a one-step AACVD process or a two-step AACVD process for use in PEC devices. Photoelectrodes were characterised by X-ray diffraction (XRD), Raman spectroscopy (RS), UV-VIS spectroscopy, and Scanning electron microscopy (SEM). The photoelectrochemical properties (PEC) of the photoelectrodes were studied in 0.5 M aqueous Na_2SO_4 and show that the best value was the BiOI deposited during 5 hours and 350 ºC (1.1 mA cm^{-2} at 1.23 V vs RHE). Although the initial goal was to obtain $BiVO_4$, both the two-step and one-step processes will have lower values regarding BiOI deposition. In the two-step process, the best value was deposition for 5h and 350 ºC (0.7 mA cm^{-2} at 1.23V vs RHE). In the one-step process, poor adhesion with the FTO produced low values.

Keywords: AACVD, $BiVO_4$ BiOI BiOBr, Photoelectrochemical Water splitting, Photoelectrode, PEC Devices.

1 Introduction

1.1 Background

In the last decades, environmental problems have become one of the principal challenges in humanity. In 2015, 17 global goals agreed by world leaders known as Sustainable Development Goals or SDGs were created. Among these goals, several related to environmental problems are clean water and sanitation, affordable and clean energy, climate action, and responsible consumption and production. Many of the ecological problems are due to the increase of the population, global economic and human well-being standards that create an immediate consumption of natural resources and the gains of the greenhouse gas emissions, principally CO_2.

Figure 1.1 Sustainable Development Goals. Extracted from the Sustainable Development Goals Report.[1]

Moreover, after the United States formed the Environmental Protection Agency (EPA) in 1979, Green chemistry took the EPA´s mandate developing different principles by asking chemists and engineers to design chemicals, chemical processes, and commercial products to protect and benefit the economy, people and the planet by finding creative and innovative ways to reduce waste, conserve energy, and discover replacements for hazardous substances. The following figure shows the 12 principles of Green chemistry:

Figure 1.2 12 Principles of Green Chemistry. Extracted from ACS chemistry for life.[2]

However, the reality of the production system is far away from these principles. The companies must compete against themselves with the principal objective of increasing their production to eliminate or absorb other competitors. In this competitive system, the main aim is economical, and generally, the environmental changes are so slow if the economic impact is harmful to the companies. Sustainable campaigns are to manipulate public opinion. Meanwhile, principal governments in the world try to have the best geographical agreements to defend the interest of their companies.

2020 will be the year remembered for the crisis of the COVID-19 and how it turned our daily lives upside down. The measures taken by the governments to control the propagation of the virus as the imposition of lockdowns around the world produced a reduction of everyday human activities. The COVID-19 pandemic dramatically impacted energy markets producing that the primary energy and carbon emissions had the most significant recession since World War II (-4.5% and -6.3%, respectively)[3]. The drop in energy consumption was driven mainly by oil, contributing almost three-quarters of the net decline, although natural gas and coal saw significant reductions. The pandemic also led to enormous economic loss. Global GDP is estimated to have fallen by over 3.5% last year – the most considerable peacetime recession since the Great Depression.

Despite this strange year, the amount of energy consumed by the world has increased throughout the last 50 years. The trend of the energy consumption during the

following years is to grow continually. The increase in the amount of energy consumption in the world is shown in Figure 1.3:

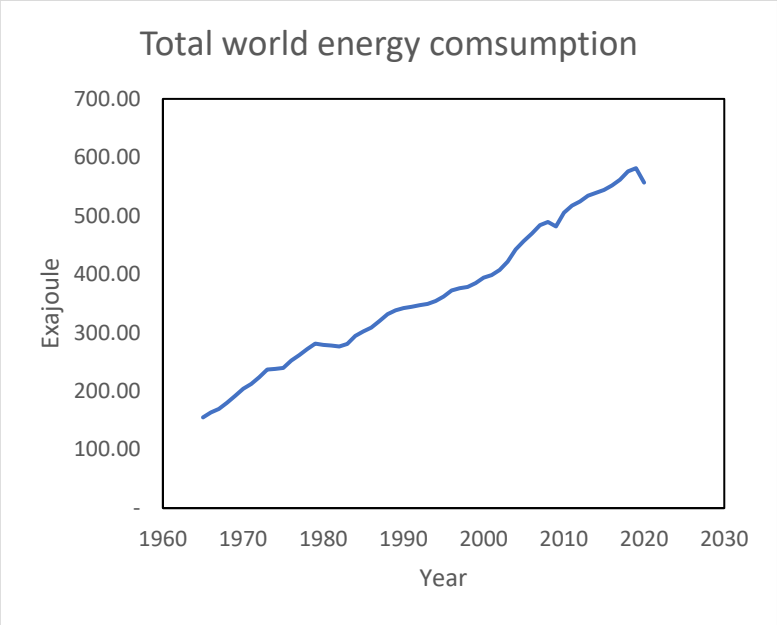

Figure 1.3 Total primary energy consumed from 1965 to 2020. Energy comprises fossil fuels (such as oil, gas and natural gas) and renewable sources of energy. Data extracted from the BP 2020 Statistical Review of World Energy.[3]

The central part of this energy comes from fossil fuels sources of energy, such as oil, natural gas, and coal. Historically the most significant energy source is oil, with 33% of the energy produced in 2019. Around the late 1990s, gas consumption overtook coal, and it was not until the 2000's that the consumption of energy from renewable sources (solar, wind, geothermal and biomass) started to be necessary. In 2020 the renewable energy, led by wind and solar energy, has increased the amount of energy produced, wind and solar capacity increased 238 GW in 2020 – 50% larger than at any time in history.[3]

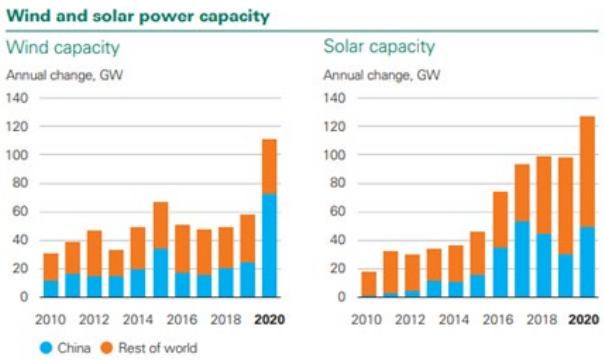

Figure 1.4 Wind and solar capacity in the last years.[3]

The use of fossil fuels and coal is the unavoidable release of greenhouse gas emissions, principally CO_2, which harms global warming and thus climate change that has an

essential impact on climate change. Equal to the energy consumption, the emissions of CO_2 by fuel in the last years has increased and the trend in the following years is to increase. In 2021, it was expected not to recover similar emissions values to pre-crisis levels. This partial recovery is due to the restrictions on transport and the continued impact of the Covid-19. For instance, the demand for coal is projected to increase by 60% more than renewables, producing a rise in emissions of almost 5%. This increase would reverse 80% of the emission generated by coal in 2020, ending up just 1.2% below the emissions levels of 2019.[4]

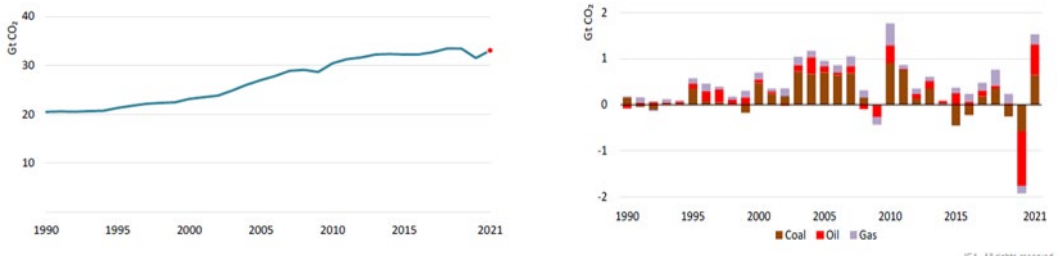

Figure 1.5 Global energy-related CO2 emissions and change in CO2 emissions by fuel.[4]

In this sense, renewable, non-polluting sources are vital to achieving this form of transformation to produce energy. In the last 5 years, renewable generation has generated around 60% of the growth in global power generation.[3] One of the most important sources is the sun; currently, different successful systems can transform solar energy into electrical energy. One of the principal problems is the electrical energy storage, so it is preferable to transform solar energy directly into a more easily transported and storage form of chemical energy by creating chemical bonds in particles as hydrogen.

1.2 Solar Fuels

One great alternative to traditional fuels from fossil sources are solar fuels. The sun delivers in one hour more energy than currently are being used from fossil fuels, nuclear power, and renewable energy sources together in one year. Using systems to transform this solar energy into fuels on a large scale could help solve the current energy problems.[5]

The sun's energy can be captured and stored directly in chemical bonds of a material or fuel to be used when needed. These products, where energy from the sun has been stored, are named solar fuels.[5]

There are two principal types of fuel:

- Hydrogen can be used either as an essential feedstock in industry or a transport fuel.

- Carbon-based fuels like carbon monoxide or methane are suitable raw materials for making a wide variety of industrial products as fertilisers, plastics, pharmaceuticals, and synthetic liquid fuels.

Providing alternatives to oil, gas and coal for transport, industry and energy generation is a critical challenge of moving from laboratory prototype systems to a large commercial scale. One of the principal challenges of solar energy is its storage, so new technologies to develop a good store are essential to have solar power available when there is poor or no sunlight. Solar fuels overcome this challenge by producing chemical bonds of the fuels.

Another challenge is transporting this energy from where it is captured to where it is used. Solar fuels could be transposed using existing distribution networks by road, rail, or sea.

Moreover, solar fuels can be converted to electricity if combined with fuel cell technologies. An example of this is shown in Figure 1.6, theoretical daily use of solar H_2 in which both storage and transportation are developed in a large-scale industry environment for vehicles and generation of electricity.

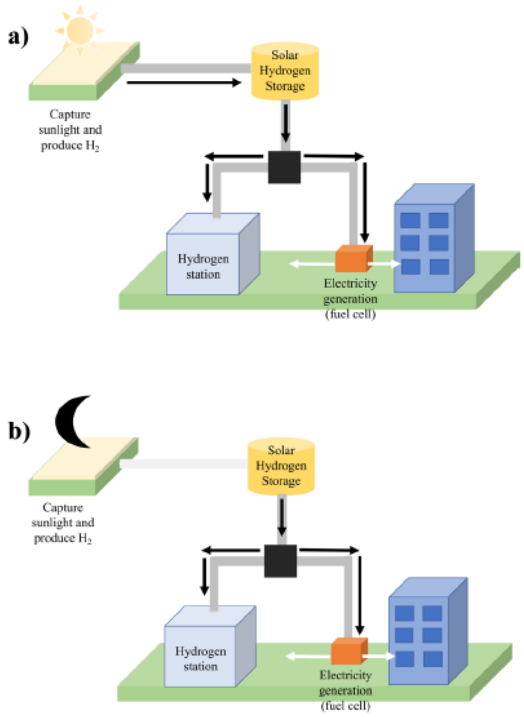

Figure 1.6 Schematic representation of a possible productive facility of solar fuels. a) At daylight conditions, solar H2 is produced and can be either stored or used. (b) At night or cloudy periods, only stored solar H2 is used. Adapted from ref.[5]

The best example of solar fuel is hydrogen, widely used as feedstock in the industry. Hydrogen is one of the most promising fuels, and it can be used in a total sustainable energy system. The higher heating value of the hydrogen is 141 MJ/Kg at 298 K, and the lower heating value is 120 MJ/Kg at 298 K, which is higher than most fuels. Hydrogen gas has a low energy density by volume versus hydrocarbons and a relatively good energy density by weight. Also, it is necessary larger tank to store. It can escape through materials and produce mechanical degradation, and it is a gas that is very flammable with a low ignition temperature.[6]

1.2.1 Current methods of hydrogen production

Nowadays, hydrogen generated from fossil fuels is the principal production source.[7] The steam reforming process of methane has an efficiency between 65%-75%, and it is the predominant method of hydrogen production, followed by coal gasification and water electrolysis.[7,8]

Although hydrogen does not produce carbon emission at the end-use point, some ways to produce hydrogen generates emissions that must be considered.[8,6]

Several methods of the production of hydrogen are[7]:

Hydrocarbons Reforming Technology

This technology is the principal method to produce hydrogen principally for refineries. Hydrocarbon reforming can be divided into:

- Steam reforming process
- Partial oxidation process
- Auto-thermal reforming process

In steam reforming, high CO emissions are generated with the steam of hydrogen, so the conditions of temperature y pressure must be improved to maximise hydrogen production and reduce carbon formation.

Gasification

It is a thermochemical process with high temperature with an organic part as coal and a gasifying reactive, generally oxygen, steam or air. A second process is necessary to separate hydrogen and convert carbon monoxide into carbon dioxide.

Pyrolysis

Hydrogen is produced with the decomposition of organic substances by heat. The temperature of operation changes depending on the organic source. Since air and water are not used, carbon oxides do not appear in the products. The biggest problem is the fouling by the carbon formed, but it can be reduced using a good reactor design.

Hydrocarbons Reforming Assisted by Using Plasma Technology

It is the technology with the best energy efficiency to produce hydrogen and is classified into thermal and non-thermal plasma. The principal difference between these two methods is the temperature of the gas. Thermal plasma can be applied to applications that require high temperature, such as gasification of solid fuels; meanwhile, non-thermal plasma is better for hydrocarbons reforming and producing syngas.

Hydrogen Production Using Ammonia [NH3] in Plasma Decomposition

The hydrogen produced with this method has a purity of 99,999% with normal pressure-temperature conditions and without using a catalyst. For the moment, it is a novel technology with an excellent perspective for producing purified hydrogen from ammonia. For instance, Prof. Shinji Kambara, Japan, Division of Environmental and Renewable Energy Systems, in collaboration with Sawafuji Electric Co., Ltd have been

studying a new hydrogen production using ammonia by using a DBD plasma reactor for fuel cell with a low cost, low environmental damage and high production efficiency.

Water Electrolysis

Hydrogen is generated by passing an electrical current through two electrodes in water. These types of technology are showed a high cost on a large scale. There are three types of different water electrolysis:

- Electrolyte alkaline
- Proton Exchange Membrane
- Solid oxide electrolysers

The electrolyte alkaline method is the most common compared with the other two water electrolysis systems. The solid oxide electrolysers are still under development with some challenges as corrosion, thermal cycling, seals and chrome migration, but it is the most electrically efficient.

Biomass

Biomass can also be used as a renewable energy source to generate hydrogen. This technology can be divided into gasification and pyrolysis (followed by the reforming process). The conditions in the process as temperature, heating rate, particle size or reactor system have high relevance in the amount of hydrogen produced.

In the last year, another biomass method to produce hydrogen using biological technologies have been developed. It has been investigated with anaerobic bacteria in a dark fermentation process or algae in the light in a photo fermentation process. This new method has a low environmental impact and a high hydrogen production efficiency.

Thermolysis & Thermochemical Water Splitting

In these processes, thermal energy is used to split the water. The water has a decomposition temperature of 2000 ºC; this implies that the materials must be resistant to high temperatures.

The difference between these two methods is that thermochemical water splitting is a combined thermolysis water splitting process with chemical reactions to reduce the water decomposition to 900ºC.

Photonic

The source of energy to produce hydrogen is photon energy. It can be classified into two different methods:

Photocatalytic Water Splitting and photoelectrochemical water splitting (PEC).

Photocatalytic water splitting is a direct method where a powder photocatalyst is dispersed in an aqueous solution to produce hydrogen from water using light. In Photoelectrochemical water splitting, an external bias based on solar energy is applied between electrodes to trigger the redox reactions at room temperature in two different electrodes, facilitating the separation of both gases once produced. The hydrogen produced is highly pure, a requirement in a fuel cell. Different photoelectrodes materials like TiO_2 $BIVO_4$ or WO_3 have been investigated to use in the method.[7.9]

These two technologies are under development and only exist in lab-scale configurations, although some analysis studies have demonstrated their potential in large scale applications.[9] Both technologies will be discussed in more detail in the next section, particularly photoelectrochemical water splitting.

2 Photoelectrochemical water splitting (PEC)

This section explains the fundamental parameters of the PEC water splitting process.

2.1 Introduction

The storage of solar energy through photoelectrochemical water splitting is one of the promising technologies to be an effective solution to the global problem of sustainable energy production. PEC water splitting for hydrogen production has been widely investigated since Fujishima and Honda discovered the electrochemical photolysis of water using TiO_2 as a photoanode connected to a platinum electrode.[10] Despite the advances today, no industrial or commercial system exists to produce effectively solar hydrogen. The main problems of photochemical water splitting are physical, chemical and engineering due to converting photons into electrons that can drive reactions with well separated and defined products.[11]

The process is based on transforming light energy (photons) into electricity using 2 electrodes immersed in an aqueous electrolyte of which one of the electrodes is a semiconductor able to absorb light to form an excited electron-hole pair.[12,9] One of the

advantages of this process is that oxygen and hydrogen are produced simultaneously in different electrodes.

Separate production allows greater control of the process avoiding safety problems and subsequent treatment to separate the gases that make the process more expensive. The purity of the hydrogen produced is an essential requirement for fuel cells. Furthermore, the process can be carried out at room temperature, so photochemical water splitting devices could have applications on a large scale.

Another advantage of the process is that the materials in the system can be constructed from inorganic products, so an improvement in the resistance of the materials, more excellent durability and less degradation is achieved.[13,9]

2.2 General explication of the process

There 2 approaches for photocatalytic water splitting:

- Basic methods where a powder photocatalyst is dissolved in an aqueous solution
- Photoelectrochemical methods (PEC)

Basic photocatalyst systems are heterogeneous processes with 2 active phases, a photocatalyst solid and an aqueous solution. This configuration is simple, and the water splitting to produce hydrogen occurs irradiating the photons to the solution with the solute dissolved. However, this process presents problems as pH changes, mainly when a scavenger is used, problems with light absorbance by the suspended particles, generation of H_2 and O_2 together and secondary reactions such as the reduction of O_2 to form superoxide (O_2-).[14,15] On the other hand, PEC systems do not present these limitations, although this method has other challenges like bad stability of the materials, low efficiency. Some studios on a large scale in both configurations have demonstrated that particle systems have a low cost of hydrogen production, but this cost is higher due to the safety concerns involved in the process and the post-treatment to separate the hydrogen from the oxygen.[9] Alternatively, PEC systems can be easier to scale up with fewer safety concerns despite the principal limitations are the low efficiencies and the reduced lifetime of the materials used. This is because some of the main properties of the photoelectrodes depend on factors that are either difficult to control or not well understood. An example of this problem is the creation of impurities during material synthesis. Optimising the synthesis is crucial for developing materials on a large scale, primarily when low-temperature and low-cost methods are used.[13]

2.3 Semiconductor properties

Semiconductors, according to molecular bonding theory, are materials with a valance band (VB) (highest occupied molecular orbital) and conduction band (CB) (lowest unoccupied molecular orbital), which correspond to the bonding and anti-bonding energy levels separated by an energy gap (Eg). The bandgap energy is defined by the energy difference between CB and VB, and its value is usually in the range of 1-5 eV.[11,16] There are two types of optical band gap transitions depending on the nature of the electronic properties of the semiconductor:

Direct transition: The lowest point of the CB is situated at the same k-vector as the highest point in the VB. In this case, the crystal momentum is maintained when a change of energy occurs.

Indirect transition: The lowest point of the CB is situated at a different k-vector to the highest point in the VB. Crystal momentum appears with the change of energy. These transitions require the absorption or emission of a photon, and the probability of it occurring is less.

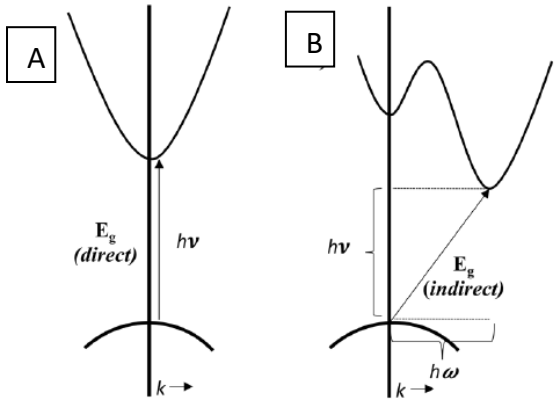

Figure 2.1 Simplified band diagram of a semiconductor. (A) Direct band gap transition. (B) Indirect band gap transition. Adapted from ref.[13]

At zero kelvin, the energy states of the CB are mostly empty of electrons, whereas the energy levels of the VB are filled up to maximum energy, the Fermi level (Ef).

The excitation by an external energy source with energy equal to or greater than the band gap energy (Eg) produces a jump of electrons from the levels of the VB to the levels of the CB, leaving the same number of holes in the VB. This is the case for intrinsic or un-doped semiconductors where the Ef is placed at the mid-gap position between VB and CB. On the other hand, doped semiconductors with impurity atoms have additional energy levels in their electronic configurations. Suppose the

semiconductor has impurities atoms with a more significant number of valence electrons than the standard configuration. In that case, it results in an electron-rich semiconductor (n-type, donor-doped semiconductor).

In contrast, if the impurities atoms of the semiconductor have fewer valance electrons than the normal material, it results in a hole-rich semiconductor (p-type, acceptor-doped semiconductors). In some cases, the defects present in the configuration define the electronic character of the material. For doped semiconductors, the number of free electrons and holes depends on the level of doping rather than the thermal excitation of electrons and holes in the band gap producing a change in the position of the Fermi level.

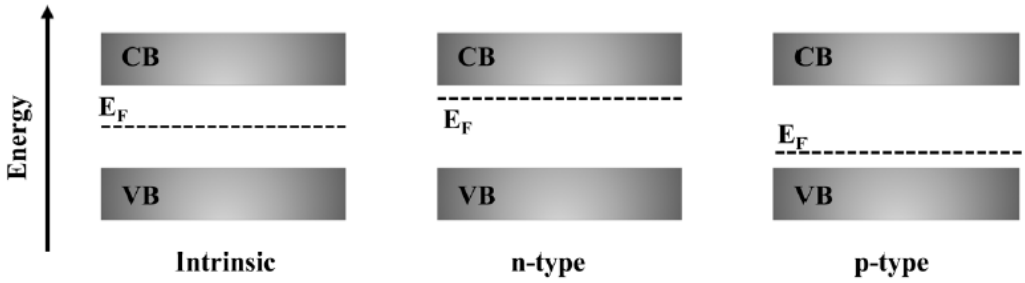

Figure 2.2 Band diagram of an intrinsic, p-type and n-type semiconductor. Adapted from ref[11]

2.4 Space charges and band bending in the semiconductor-electrolyte interface

The semiconductor in contact with an electrolyte creates an electric current that initially flows across the junction semiconductor-electrolyte until electronic equilibrium is reached where the Fermi energy of the electrons in the semiconductor (Ef) is equal to the redox potential of the electrolyte (E_{redox}). This transfer of electronic transfers produces a region at the semiconductor-electrolyte with a charge distribution different from the bulk material, known as the space-charge layer, at the semiconductor side, and electrolytic double layer at the electrolyte side, which is divided in the Helmholtz layer and the diffuse Gouy-Chapman layer. The diffuse Gouy-Chapman layer is the region where water molecules surround the ions present in the solution. The Helmholtz layer is the region closest to the semiconductor, formed principally for adsorbed ions and low ions in the solution.[13,17]

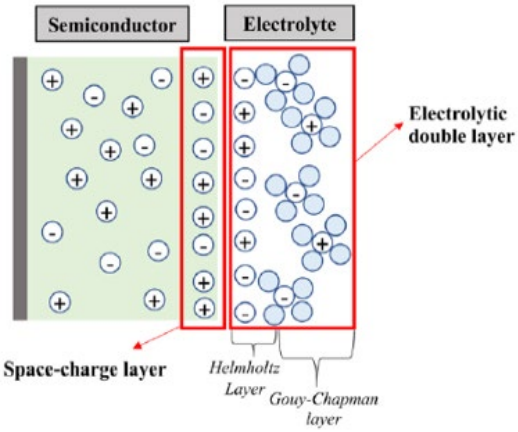

Figure 2.3 Schematic diagram of the semiconductor-electrolyte interface. Space-charge layer and electrolytic double layer. Adapted from ref.[13]

A band bending of the CB and VB is necessary to achieve an electronic equilibrium in the interface of the semiconductor-electrolyte. On the junction region of the semiconductor, the band bending depends on the position of the Fermi level in the semiconductor. There are 4 situations possible:

Flat-Band potential (U_{fb}): When there is no excess of charges on either side of the junction, and the bands are flat, a space charger is not formed, and an electric field is not generated.

Accumulation layer: when an excess of positive (negative) charges is adsorbed at the surface of an n-type (or p-type) semiconductor, it produces a downward (upward) bending of the CB and VB towards the interface. Free majority carriers create the accumulation layer near the surface to compensate for these surface charges.

Depletion layer: If there is a transfer of an excess of positive (negative) charges from the surface of the n-type (p-type) semiconductor to the electrolyte, produce an upward (downward) bending of the CB and VB towards the interface. Opposite charges species must compensate for the number of charges in the depletion layer at the material's surface.

Inversion layer: n-type (p-type) can become p-type (n-type) if the number of negative (positive) surface charges adsorbed increases the Fermi level crosses the middle of the band gap and a downward (upward) band bending of the CB and VB is formed.[13,17]

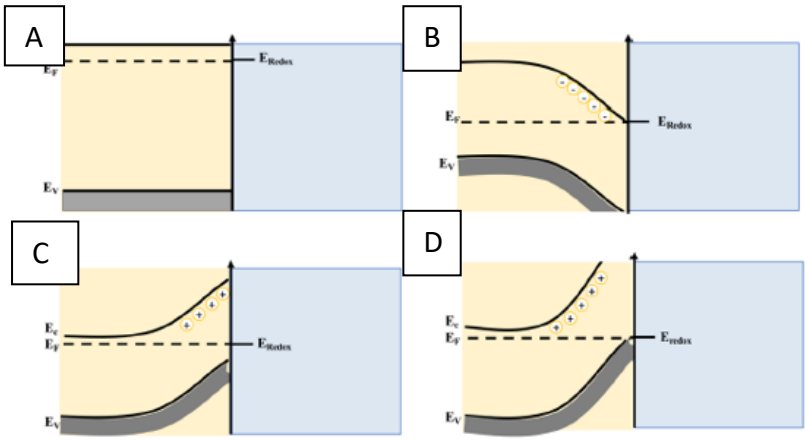

Figure 2.4 Electronic energy levels of an n-type semiconductor in contact with an electrolyte. (A) flat band potential, (B) accumulation layer, (C) depletion layer and (D) inversion layer. Adapted from ref.[17] Copyright 2001 Springer Nature.

In addition, the effect on the bad edges of the semiconductor of an applied bias or a change in the pH must be considered.

An external bias can be applied to obtain the potentials required to undertake the water reactions through the photoelectrode and the counter electrode. The charges in the space layer are modified when an external bias is applied, and the semiconductor's band bending is also limited.

The position of the band edges depends on the pH of the solution, about 59 mV per pH unit concerning the redox potential in the electrolyte. However, this is not a helpful property due to the reduction and oxidation potentials of water also depend on the pH for the Nest

$$E_{red} = E^0_{red} - \frac{RT}{4F} ln\left(\frac{p^2_{H2}}{[H^+]^4}\right) = E^0_{red} - \frac{2.3RT}{F}\left(\log\left(p^{\frac{1}{2}}_{H2}\right) + pH\right) \quad 2\text{-}1$$

$$E_{ox} = E^0_{ox} + \frac{RT}{4F} ln(p_{O2}[H^+]^4) = E^0_{ox} + \frac{2.3RT}{F}(\log(p_{O2}) - pH)$$

2.5 Fundamentals of photoelectrochemical water splitting

The mechanism of the PEC water splitting begins with the absorption of a photon in the semiconductor material; this energy must be equivalent to or greater than its band gap to form excited electron-hole pairs. The energy requires a minimum Gibbs free energy of 237 kJ mol^{-1}.[16] The electrons (e^-), which are in the valence band (VB), are exited into the conduction band (CB), producing the creation of holes (h^+) in the VB. At this moment, the system lost the condition of equilibrium, especially at the space-charge region, and quasi-Fermi levels appear for e^- and h^+, instead of having a unique

Fermi level in the semiconductor-electrolyte junction, which moves its position downward or upward for a p-type or n-type semiconductor, respectively.[18,19,13]

Regardless of the configuration used in the process, the overall mechanism of the water splitting is the next[18,9,10]:

1) The material's absorption of light with an energy equivalent to or greater than the band gap of the semiconductor material to form excited electron-hole pairs.

2) Separation and migration of these photocarriers to the photocatalyst surface trying to avoid recombination in the bulk or surface, which can appear if there are defects on the surface of the semiconductor avoiding the migration of the photocurrents within the space charge layer. In basic systems, both photocarriers migrate to the surface, but in PEC systems, band bending at the semiconductor/electrolyte interface is the driving force to separate photogenerated carriers; one of the photocarriers migrates to the surface-electrolyte interface of the photoelectrode while the other carrier migrates to the counter electrode in the external circuit.

The efficiency of the generation and separation of photocurrents depends on the penetration depth of the light on the surface, the width of the space charger region and the diffusion length of the minority carrier.

3) The holes drive the oxygen evolution reaction (OER) in one of the surfaces while the electrons produce the hydrogen evolution reaction (HER) at a separate surface or electrode. In an n-type semiconductor photoanode, electrons go to the cathode, where the HER is produced. Meanwhile, the OER occurs on the photoelectrode photoanode. In a p-system semiconductor photoanode, the holes flow to the anode, and the HER occurs on the photoelectrode surface. Associated with driving the kinetics of the HER and OER, there are overpotentials at the solid-liquid interface. Minimising these overpotentials is a crucial step to creating efficient water splitting devices. In addition, overpotential, entropic losses with the generation of electrons and holes and other parasitic losses must be considered in the band gap requirement. Considering these losses, the driving force for water splitting is always higher than the material's band gap. The bandgap needs to be enough to provide the energy necessary to split the water and must be as small as possible to have the capability to absorb a significant portion of the solar spectrum.

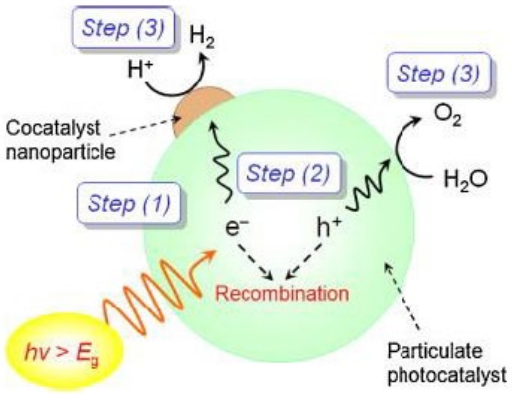

Figure 2.5 photocatalytic overall water splitting on a semiconductor particle. Adapted from ref.[18] Copyright (2007) American Chemical Society.

To inject h^+ and e^- into the solution, the energy levels must exceed the electrochemical redox potentials for the OER and HER. For this reason, the potential of CB of the semiconductor at the semiconductor/liquid junction must be more negative than the reduction potential of H^+ to H_2 (0 VNHE at pH=0); meanwhile, the VB must have a more positive potential than the oxidation potential of H_2O to O_2 (1.23 VNHE at pH=0).[9] Figure 2.6 depicts a schematic illustration of band structures of some photocatalysts, which presents the above described:

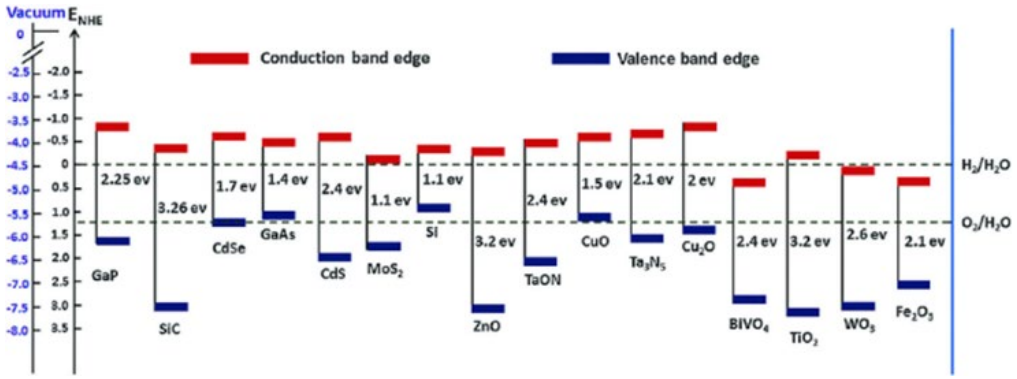

Figure 2.6 Band edge positions for a range of semiconductors. Adapted from ref.[21]

2.6 PEC cell configurations[20,16]

A PEC water splitting system mainly is formed for an electrode or photoelectrode, a cathode or photocathode and electrolyte. In the PEC systems exist 2 types different of configurations depending on the number of electrodes used:

Two-electrode systems form a counter electrode, usually platinum and the working electrode, which contains the photocatalyst of interest.

Three-electrode systems with a reference electrode coupled with the other two electrodes described in the two-electrodes system.

Different Setups for the PEC water splitting exist depending on the electrode configuration:

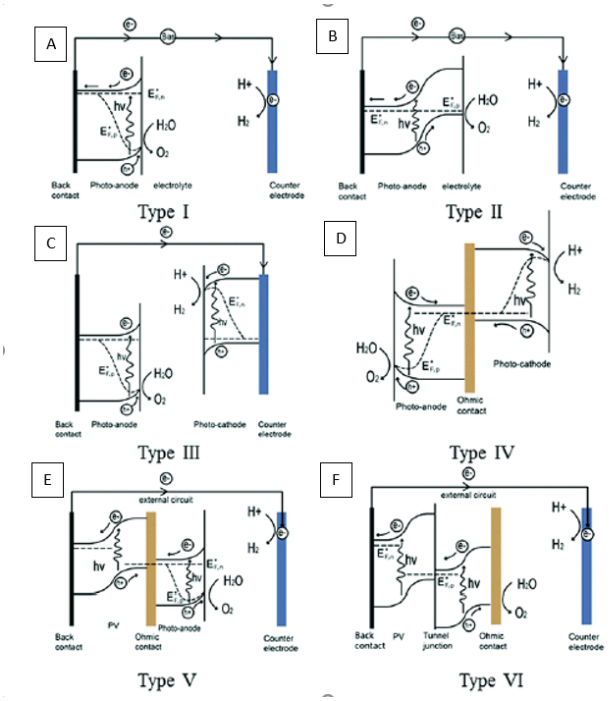

Figure 2.7 PEC devices configurations: (A) type I, (B) type II, (C) type III, (D) type IV, (E) type V, (F) type VI. It is reproduced from ref.[16] Published by The Royal Society of Chemistry.

The simplest configuration is the type I. This configuration only contains a metal counter electrode and one semiconductor light absorber, which can be used either as a photoanode or photocathode to carry the water splitting oxidation or reduction reaction. An external bias is needed for one semiconductor light absorber to trigger the separation of the photocarriers throughout the cell.

Type II or heterojunction photoelectrode Pec device. Two semiconductors are coupled in only one electrode in this system to create a heterojunction. For instance, an n-type semiconductor couple with a p-type semiconductor is a heterojunction system. A space-charger layer is formed at the interface of both surfaces producing the diffusion of photocarriers between them. Depending on the alignment of the bands in the n-type and p-type semiconductors, e^- and h^+ can diffuse the different forms. In the example shown in Figure 2.7 B, holes migrate from the n-type semiconductor's VB to the p-type semiconductor's VB. Meanwhile, the electrons migrate from the CB of the p-type semiconductor to the CV of the n-type semiconductor. The advantages of this setup are the better separation of the charges, a bigger lifetime of the charges, higher

reaction rates and an increase in the light absorption when the alignment of the bands have the correct positions.[24]

Type III and type IV utilise a photocathode and photoanode connected in series in a tandem configuration. A conductive metal wire is used for the setups of Figure 2.7 C, and the setups of Figure 2.7 D, a wireless setup, is used in which a transparent conductive substrate is used as an ohmic contact. To ensure a complimentary light absorption where the second material should absorb the photons from the first material, the CV minimum of the photoanode must be more negative than the VB maximum of the photocathode. The principal advantages of these configurations are higher photovoltage and a significant range of materials used in the tandem. However, both parts of the tandem must maintain a similar current density when an external bias is not applied.

Type V device configuration combines a PEC system with a photovoltaic cell. The additional energy necessary to split the water is supplied by the photovoltaic cell, increasing the range of materials used in these systems. A transparent oxide layer protection between them is necessary to provide a recombination layer of the holes from the photovoltaic cell and the electrons from the PEC system (only for n-type configurations).

Type VI configuration is a combination of a photovoltaic cell with an electrolyser. The photovoltaic cell supplies the energy, and the electrolyser performs the water splitting. Even though it is not a PEC system in practice, this configuration can be considered because the reactions occur inside the cell.

2.7 Photoelectrode materials in PEC devices

Despite 50 years of investigation from the discovery of PEC water splitting, creating a large-scale process with enough efficiency using visible light is still a long way, so the investigation is essential. The principal problem is to find a semiconductor material able to satisfy all the requirements that need to be accomplished in a large-scale system:[13,16,23]

- Position of the band gap (Eg): The position of the band gap should be in the range of the visible spectrum to maximise the absorption of light. Natural light is formed by 5% of UV (399-400nm), 43% visible (400-700 nm), and 52% infrared radiation (700-2500nm).[16] The optimal band gap in PEC devices is in the range of 1.9 and 3.1 eV, which corresponds to the range of 400-650 nm. The minimum band gap requires enough energy to split the water (1.23 eV) and all the losses and overpotentials

generate during the process.[16] The theoretical maximum solar-to-hydrogen (STH) efficiency is determined by the position of the band gap of the semiconductor. The highest STH efficiency corresponds with the lower value of the band gap due to the larger absorption of the solar light.

- Charge transport efficiency in the semiconductor: Photocathode materials: Recombination is the major problem in the low STH efficiency. Thus, it is necessary to investigate better structures (crystallinity, nanostructure and hole electron mobility) to avoid recombination and promote efficient charge carrier separation and transport.[13,16]

- Stability in an aqueous electrolyte in the dark and under light illumination: The material must be electrochemically, photoelectrochemically and chemically stable in the solution. Many non-oxide semiconductors dissolve or form a thin oxide layer at the surface in contact with the electrolyte solution producing problems in the charge transfer across the junction interface. In these conditions, metal oxides are more stable, but they can suffer from photocorrosion, particularly metal sulphides, by the holes generated rather than the water. This photocorrosion depends upon the relative positions of the band edges and the respective decomposition potentials.

- The band edges position must straddle the redox potentials of the photocatalytic reaction for the hydrogen and oxygen half-reactions: A limited number of semiconductors meet this requirement, which often requires large band gap positions. One advantage of the PEC devices is that only one of the half-reactions for water splitting is needed; therefore, a bigger range of materials can be used. The conduction band must be more negative than the H_2 generation potential, and the valence band more positive than the O_2 generation potential to produce the overall water splitting.

- Low overpotentials for the reactions: The overpotentials should be as low as possible, so the charge transfer should be fast to avoid recombination by accumulating charges at the surface. The combination with other materials has been extensively studied to minimise these problems.

- Low-cost and sustainable: To meet the global sustainable development, the materials utilised should be cheap, abundant, and ideally prepared via a green synthetic route.

3 Bismuth vanadate as photoanode in PEC devices

3.1 Description

Bismuth vanadate is a promising n-type semiconductor for photocatalytic water splitting. Since the discovery of the PEC Photoelectrochemical (PEC) water splitting by Honda-Fujishima[10] in 1972 using TiO_2 as photoanode, a career to discover new materials with the ability to reproduce the natural photosynthesis artificially to produce hydrogen by splitting the water under a source of light and understand the mechanism of this technology started.

Solar water splitting is a process that requires a minimum Gibbs free energy of 237 kJ mol^{-1}.

Kudo *et al.* reported the first use of $BiVO_4$ as photocatalyst under visible light irradiation for O_2 evolution in an aqueous $AgNO_3$ solution.[24]

3.2 Crystal and electronic structures of $BiVO_4$

$BiVO_4$ can adapt 3 different polymorphic forms: orthorhombic crystal structure (pucherite), tetragonal zircon (t-z) (dreyerite) and monoclinic scheelite (m-s) (clinobisvanite) structure.[26-30] Besides, another tetragonal scheelite (t-s) structure exists with different atomic positions in the clinobisvanite forme.[27,28] The Table 3.1 shows the difference in the crystal structure and the bond length in the different polymorphs of $BiVO_4$.[27,28]

Although $BiVO_4$ in pucherite forms has not been prepared in normal laboratory routes, the other 2 forms can be synthesized as shown in Figure 3.1. The zircon-type structure has been reported with low-temperature synthesis.[27] However, the structures achieved at low temperatures may vary depending on the methods used for the synthesis as kinetic is a critical parameter. The monoclinic scheelite can be produced from tetragonal zircon with a high temperature in an irreversible process, and a reversible transition between the tetragonal scheelite and monoclinic scheelite appears at 255 °C (528 K).[28]

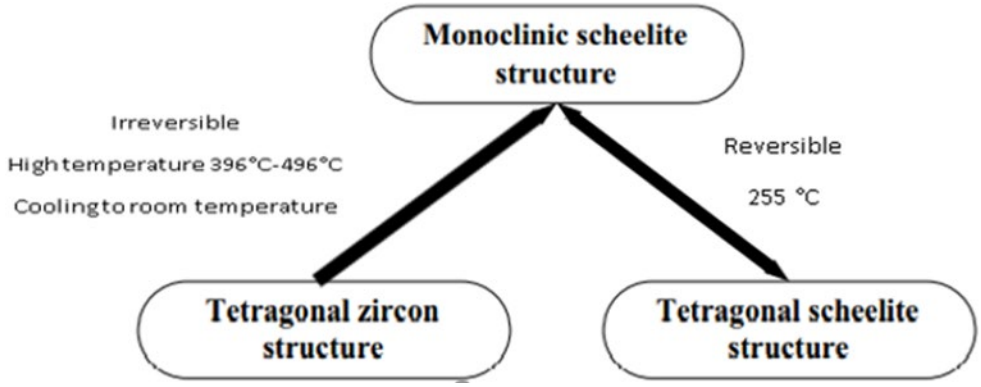

Figure 3.1 Phase transition of $BiVO_4$ in normal laboratory routes.[27,28]

Table 3. 1 Crystal structure and bond length of the different $BiVO_4$ forms.[27,28]

Crystal System	**Orthorhombic**	**Tetragonal Zircon**	**Monoclinic Scheelite**	**Tetragonal Scheelite**
Crystal structure (Å)				
Space group	*Pnca*	*$I4_1/amd$*	*C_2/c*	*$I4_1/a$*
a	5.332	7.303	7.2472	5.1470
b	5.060	7.303	11.6972	5.1470
c	12.020	6.584	5.0898	11.7216
Bond length (Å)				
Bi–O	2.20	2.41	2.35	2.40
	2.31	2.55	2.37	2.47
	2.53		2.52	
	2.73		2.63	
V–O	1.76	1.7	1.69	1.72
	2.73		1.77	

The scheelite $BiVO_4$ possesses enhanced photoactivity better than zircon-type mainly due to the band gap energies (2.4 eV and 2.9 eV, respectively), resulting in a best photon absorption. This difference in the band gap is due to the charge transfer transition from O 2p orbital to the empty orbital V 3d; meanwhile, the scheelite

structure has a reduced band gap as the 6s state of $Bi3^{+}$ appears in a position above the O 2p and the transitions are between Bi 6s2 or a hybrid Bi 6s2-O 2p orbitals to the V 3d.[27,30] There are also differences among $BiVO_4$ scheelite structures despite having the same band gap. Monoclinic scheelite structure shows better results in photocatalytic activity because it presents a severe distortion. The Bi and the distorted octahedron of oxygen are coordinated, and the VO_4 tetrahedra and BiO_8 dodecahedra distortion produces the apparition of two and four oxygen atoms in each subunit. With this overlap of O 2p and Bi 6s orbitals in the valance band (VB), the mobility of photogenerated charge carriers results in improved photocatalytic activity.

Today, there is an open debate about if the $BIVO_4$ is an indirect or a direct bandgap semiconductor material. The major part of the studies suggests that it is an indirect bandgap because this material possesses two high lines of symmetry of the Brillouin zone. However, recently Zhao et al.[31], with DFT calculations, has found that Bi and O atoms interactions in the BIO8 dodecahedron produce non-bonding states at the top of the VB and the bottom of the CB. Payne et al.[32] have also shown the asymmetry and the interaction of O 2p in the upper edge of VB and The Bi 6p in the middle of VB, producing a Bi lone pair. Moreover, the DFT calculations by Walsh and Zhao have exposed that the effective masses of holes and electrons is lower compared to some commercial semiconductors as TiO_2.[27]

For water splitting applications, the monoclinic $BiVO_4$ is the most active one with a theoretical maximum photocurrent of 7.4 mA cm^{-2} at 1.23 V *vs* 1.23 V *vs* RHE and STH efficiency of 9.1 %.[16]However, the efficiency of $BiVO_4$ is limited for different drawbacks: at low potentials possess a relatively low IPCE value, suffers from rapid photocarrier recombination as a result of short electron diffusion length (with only 10 nm) that affects its apparent quantum efficiency directly, photocurrent stability is not very good due to form a dissolution of V^{5+} ions in the solution and reactions in the surface of the photoelectrode such as O_2 and H_2O_2 that act as centres where there is recombination and is a material that suffers for a slow hole transfer kinetic producing a poor surface water oxidation.[27,16] Some studies of Electrochemical impedance spectroscopy (EIS) show that bare $BiVO_4$ possess a poor kinetic charge transfer due to a more significant resistance for electrons to crossing the interface between the electrode and the electrolyte, which produce the accumulation at the CB of the electrons and with the time recombining with holes in the VB resulting in a decrease in its efficiency.[26]

Much effort has been developed with different modifications to solve or reduce the effect of these problems in water splitting applications. In this regard, 4 types of modification have been done to improve the photocatalytic properties of $BIVO_4$:[26,27]

- Facet control dependence of $BiVO_4$
- Control of the morphology
- Forming composite heterojunctions
- Doping elements

4 AA(CVD) PROCESS

In this section, the fundamentals, mechanisms and differences of the chemical vapour deposition (CVD) and Aerosol chemical vapour deposition for the preparation of thin films are summarised. Although both processes are quite similar, specific differences mark the parameters to consider in both methods.

4.1 Fundamentals of the CVD process

Chemical Vapor Deposition is a versatile technique used for the deposition of gas-phase reactants (percussors) on a heated substrate material by dissociation and/or chemical reaction occurring in the vapour-phase (via homogeneous reactions) or in the surface (via heterogeneous chemical reactions) of this heated substrate creating solid in its.[33,34] The resulting solid deposit in the surface is in the form of powder, single crystal, or thin film.[33]

This technique can be used to deposit on to large surfaces and offers good film uniformity, composition control and excellent step coverage. It can be used to deposit highly dense films and pure with good adhesion. In the CVD process, the properties of the thin films are controlled by changing different parameters like temperature, deposition rate, components of the gas phase, physical conditions of the gas phase, the solid surface.[35] The applications of this process are very widely since film applications like dielectrics conductors, passivation layers or oxidation barriers until preparation of high-temperature materials or the production of solar cells.[33]

The steps of the process can be summarised in the following key steps:

Firstly, precursors active gaseous are generated by evaporation and transported into a reaction chamber utilising either a carrier gas (argon, nitrogen, air or vacuum). In the heated chamber, the decomposition of the precursor molecules occurs, generating reactive intermediates and gaseous by-products on the surface. At a high temperature above the temperature of decomposition of the intermediate species, homogeneous reactions in the gas phase appear and producing an undergo subsequent

decomposition and/or chemical reactions that create powder and volatile by-products. The deposition of these types of film may have poor adhesion. At temperatures below the decomposition of the intermediate species produce a diffusion or convection of these intermediate species across the boundary layer and undergo the following steps:

The gaseous reactants are adsorbed onto the heated surface producing a heterogeneous reaction at the gas-solid interface, which produces the subsequent nucleation of the atoms, leading to film growth and forming a crystallisation centre.

Finally, the desorption and mass transport of the by-products away from the deposition chamber allows the production of films of the desired product.[34,35,36] This process is illustrated in Figure 4.1

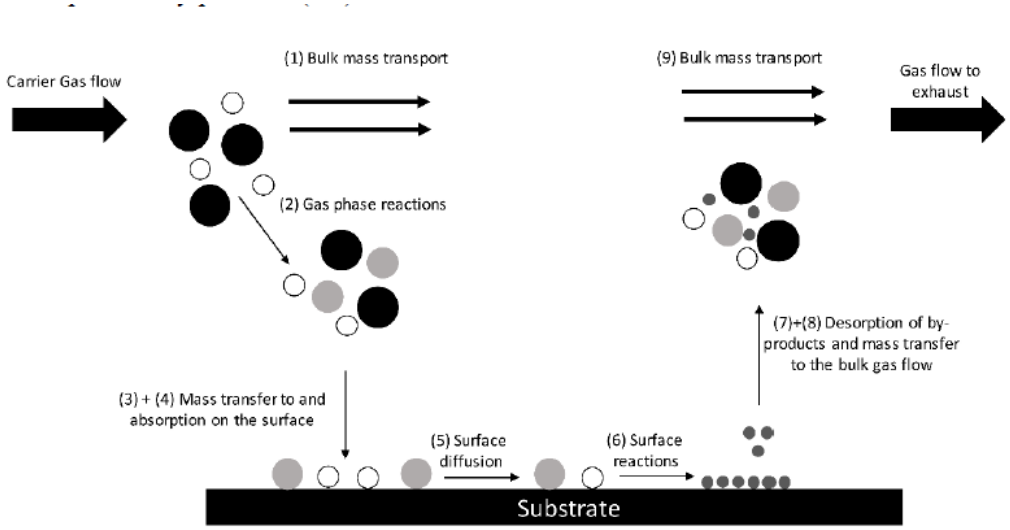

Figure 4.1 Schematic diagram of a conventional CVD process. Adapted from ref.[37]

4.2 Historical evolution

Since the first industrial application of CVD in 1893 when lodyguine produced a deposition of W onto carbon lamp filaments through the reduction of WCl_6 by H_2. In this period, CVD was developed as an economical industrial process in the extraction and pyrometallurgy to produce high purity metals like Ni, Zr and Ta. In the last 60 years, the applications of CVD have been improved with consideration of the deposition aspects of the process. With these changes, CVD has been converted into an essential technique in coating technology for the productions of functional semiconductor films and coatings with properties as protection against wear, oxidation, corrosion, chemical reaction, thermal shock, and neutron adsorption. Nowadays, the CVD process has much importance in military, aerospace, science, and

engineering fields. In summary, the current applications of CVD can be classified into four categories:[34]

- Surface modifications coatings.
- Extraction and pyrometallurgy.
- Electronic and optoelectronic materials.
- Ceramic fibres and ceramic matrix composites.

Only volatile and thermally stable precursors can be used in a conventional CVD process, producing a limitation in the different precursors that can be used and improved.[34,35,40]In this context, the process has been involved in different directions, resulting in a wide range of variants of the technique, such as plasma-enhanced CVD (PECVD) and photo-assisted CVD (PACVD), which use plasma and light respectively to activate the chemical reactions. Atomic Layer Epitaxy (ALE) is a variant of CVD where a monatomic layer is grown with saturating surface reaction sequence. Other variants, including Aerosol Assisted CVD (AACVD) and pulsed injection (MOCVD), use a particular generation of the precursors and delivery system contrary to the main CVD. The use of metalorganic as precursor rather than inorganic precursor is another alternative for the CVD in the metalorganic CVD (MOCVD). Other options are to use a flame source to produce the chemical reactions in the flame assisted vapour deposition (FAVD), the deposition onto porous substrates in the Electrochemical vapour deposition (EVD) and the deposition of dense ceramic matrix during the fabrication of ceramic composites in chemical vapour infiltration (CVI).[34,40]

4.3 Fundamentals of AACVD process

In an AACVD process, a solvent is used to dissolve chemical precursors. An aerosol is generated and transported by a carrier gas in a reactor chamber. It is a variant of conventional CVD process; CVD mechanisms have different problems like the selection and delivery of chemical precursors, the lack of proper volatile precursors and the difficulty in controlling the stoichiometry of the deposition.[35]

However, AACVD solves the availability and delivery problems of the chemical precursors because volatility is not an essential factor, a lot of precursors can be used, offering more possibilities to fabricate high-quality CVD products at low cost. This method involves the atomisation of a precursor solution into fine, sub-micrometre-sized aerosol droplets, which are delivered to a heated reaction zone and undergo

evaporation, descomposition, and homogeneous or/and heterogeneous chemical reactions to form the desired products. Homogeneous reaction processes occur when the temperature of the reactor chamber is too high. Meanwhile, the heterogeneous reactions process occurs when the reactor chamber's temperature is not too high.

Typically, the vaporised precursor in a heterogeneous reaction system suffers from preliminary decomposition in the gas phase. The heated surface adsorbs the resultant intermediate products on the heated surface undergoing chemical reactions/decomposition to form the desired film. In a homogeneous reaction system, vaporised precursor decomposes/reacts primarily in the gas phase giving rise to films with very fine particles and structures. Finally, diffusion of by-products to the exhaust system occurs[35,41]

A schematic image of an AACVD process is shown in Figure 4.2.

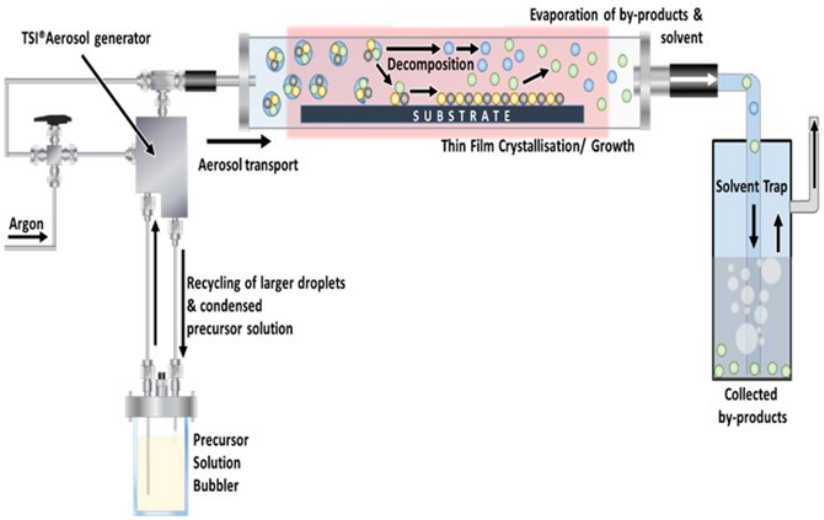

Figure 4.2 Schematic of the AACVD setup used during the experiments.

4.4 Mass-transport mechanisms

4.4.1 The boundary layer

The behaviour of the flow of the gas is controlled by fluid mechanics and is characterised by the Reynolds number (Re). In general, the gas flow is laminar, but at some points, the flow may be disturbed by convective forces and may become turbulent.

The boundary layer can be defined as the region of the tube in which the flow velocity changes from a velocity of zero at the wall of the tube to that of the bulk gas away from the wall. The thickness of the boundary layer increases along the tube from the tube's inlet until the flow becomes stabilised, as in Figure 4.3 The reactant gases must diffuse through it to reach the heated surface. The thickness of the boundary layer Δ, is inversely proportional to the square root of the Reynolds number, so the thickness of the boundary layer decreases with higher gas-flow velocity and increases with the distance from the inlet of the tube as the following equation:[33,38,39]

$$\Delta = \sqrt{\frac{x}{Re}} \qquad 4-1$$

Where: $Re = \frac{\rho u_x}{\mu}$

ρ = mass density

u = flow density

x = distance from the inlet in the flow direction

μ = viscosity

We can divide the tube into 3 zones where the boundary layer is different. The first zone exists a “plug flow” regime, where the real flow has a nearly constant velocity with a relatively thin boundary layer, which can be ignored. In the second zone, 2 different boundary layers grow until finally connected, creating an indistinct region in the third zone of the tube with a Poiseuille flow. In the second zone, the velocity, temperature, concentrations, and other parameters are relatively fixed out the boundary layers.[38,39]

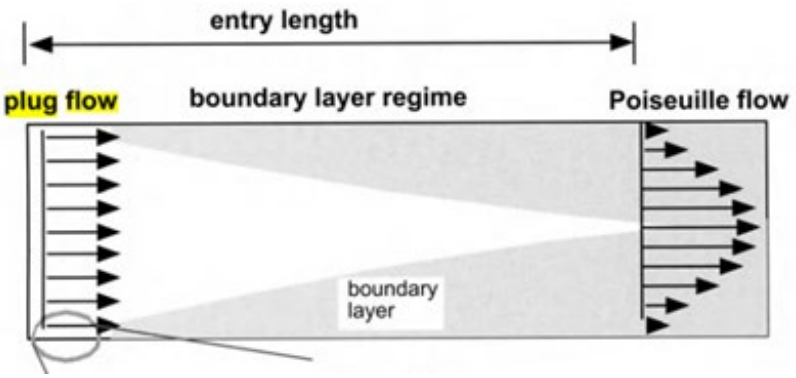

Figure 4.3 increase of the boundary layer along the tube. Adapted from.[39]

Across the boundary layer, different zones delimit where homogeneous or heterogeneous reactions occur. Figure 4.4 shows the different reaction zones. In reaction zone 5 and in the gas stream, homogeneous reactions may occur in the vapour, producing undesirable homogeneous nucleation with bad characteristics for the deposition as flaky and non-adherent coating. In some cases, these reactions are favourable when there is no homogeneous nucleation. In reaction zone 4, heterogeneous reactions occur between the phase boundary vapour/coating. These types of reactions control the deposition rate and the characteristics of the film. If the temperature is relatively high in the process, other types of solid-state reactions can occur in zones 3-1 as phase transformations, precipitation, or grain growth). In zone 1, some intermediate phases can be formed, and the reactions in this part are important to achieve good adhesion of the film on the substrate.[33]

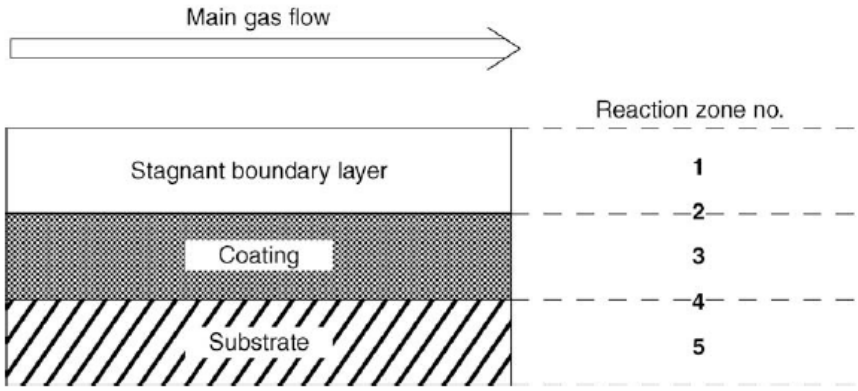

Figure 4.4 reaction zones in CVD. Adapted from ref.[33]

Equal to the velocity, there are a temperature boundary layer and a concentration boundary layer. In the case of the temperature, it is very similar to the velocity layer. The gases that flow along the tube are heated quickly when they enter into contact with the tube's hot surface, producing a steep temperature gradient. Exist an increase in the average temperature toward downstream.

The concentration along the tube becomes gradually depleted for material deposition, and the increase of the by-products gas increases in the boundary layer.

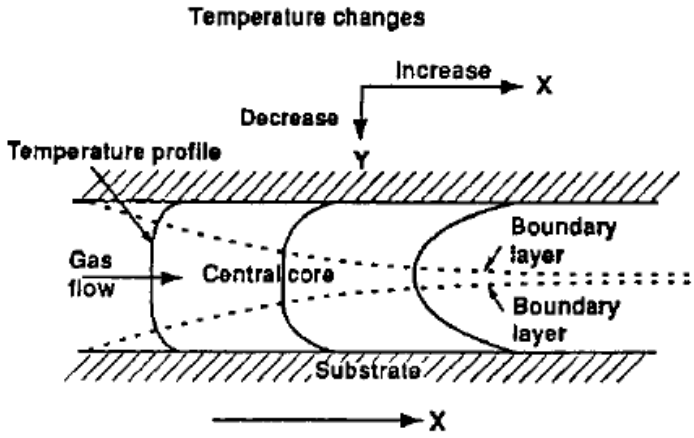

Figure 4.5 Temperature boundary layer and temperature changes in a tubular Reactor. Adapted from ref.[38]

4.5 Rate-limiting steps

In a CVD some several rate-limiting steps can be identified. There are usually ordered and discussed in five principal categories:[33,38]

- Surface reactions kinetics: This rate-limiting step occurs when the deposition rate is lower than the mass rate that enters the tube and the mass transport rate in the vapour to or from the substrate. At low temperatures, the reactions occur slowly, and there is an accumulation of reactants at the surface for the low-pressure, creating a thin boundary layer, and the reactants can reach the deposition surface easily. If the boundary layer is thin, the diffusion coefficient is not essential, and the components reach the surface with ease.

- Thermodynamic control is produced when the mass input into the reactor and the deposition rate is equal. This is produced at extreme deposition conditions as high temperatures and low flow rates.

- Mass transport control usually happens when the pressure and the temperature are high and produce a low flow that creates a thicker boundary layer. In this case, it is the phenomenon that controls the diffusion of the reactants through the boundary layer and the diffusion of the by-products in the desapsortion process. In addition, the decomposition reactions are very quickly at a high temperature.

- Nucleation control is produced at low supersaturation

- Homogeneous reactions control is produced for some species that the formation rate of key species in the vapour zone can control the deposition rate.

Although these five categories can appear and influence the result, mass control and surface kinetics are usually the rate-limiting steps that control the different processes. Surface kinetics led to achieving better results with uniform thickness on the substrate.

4.5.1 Control of the limiting step[33]

To predict the rate-limiting step in CVD, reaction resistances are usually used. Diffusion flux J_D in the boundary layer can be expressed as:

$$J_D = \frac{D}{RT}\frac{P_b - P_s}{\Delta} \qquad 4-2$$

Where R= gas constant, T=absolute temperature (K), D= Diffusion coefficient, Δ= Boundary layer thickness

The mass flux J_M towards the surface of the substrate can be expressed as:

$$J_M = \frac{1}{RT}\frac{P_b - P_{eq}}{\frac{\Delta}{D} + \frac{1}{K_m}} \qquad 4-3$$

Where δ/D and $1/k_m$ are the reaction resistances and $P_b - P_{eq}$ is the driven force.

If δ/D is much bigger than $1/k_m$, the mass transport in the vapour controls the process; meanwhile, the surface reaction kinetic control the process if $1/K_m$ is much bigger than δ/D.

As expressed in equation 4-1, the thickness Δ of the boundary layer is inversely proportional to the square root of the Reynolds number. The density, ρ, depends on the temperature and the pressure, while the viscosity, $\boldsymbol{\mu}$, and flow density, v, depend only on temperature, so the dependence of the Δ cab is expressed as:

$$\delta = \text{const}\ (T^{m/2}/p^{1/2}) \qquad 4-4$$

Meanwhile for the diffusion coefficient D is affected by the pressure and temperature according to the equation:

$$q\ D = D_{i,o}\ (p_i/p)(T/T_o)^{1.75} \qquad 4-5$$

Where $D_{i,o}$ is the value of reference of the diffusion coefficient, and p_i is the partial pressure of the specie i.

The value of the mass transfer coefficient follows the Arrhenius equation:

$$K_m = A\exp^{Ea/RT} \qquad 4-6$$

Where A is the factor preexponential and E_a is the activation energy. The surface reaction increases with decreasing temperature, in the case of the δ/D, the rise in value with decreasing temperature and increasing pressure. This increase with the decreasing of the temperature is more significant than for the case of the surface reaction.

5 Materials and methods

5.1 Research objectives

1. Study the impact of different parameters in the deposition on FTO in AACVD processes.

2. Synthesis of BIOI and BIOBr using the AACVD process and their transformation in $BIVO_4$ to study different properties and viability in PEC solar-driven water splitting systems.

3. Synthesis of $BIVO_4$ thin film on FTO in one-step AACVD process to study different properties and viability in PEC solar-driven water splitting systems.

5.2 AACVD set up

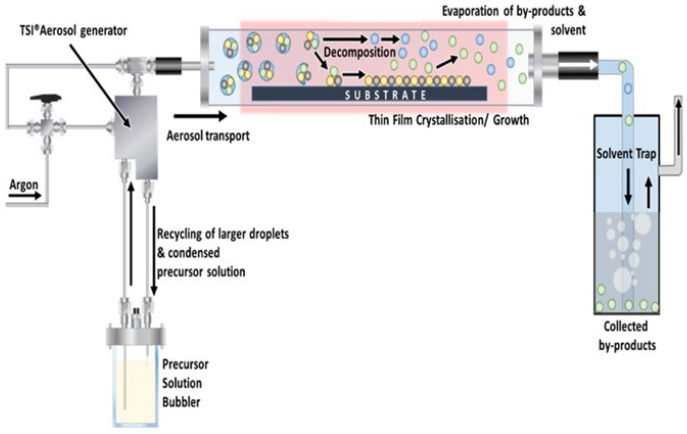

Figure 5.1 Schematic of the AACVD setup used during the experiments.

The aerosol droplets were generated using a TSI Model 3076 Constant Output Atomizer using different solutions and air or nitrogen as carrier gases at different flow rates. FTO-ABS glasses placed inside a tube furnace were chosen to be the film depositing substrate due to its good conductivity and wide range of use. The tube furnace used during the experiments was a ZS-3G Carbolite tube furnace with 3 heaters separated with unheated zone barriers and a quartz tube. Different parameters and conditions were performed to assess the growth mechanism and

optimisation. A solvent trap was situated at the end of the line to collect the by-products generated.

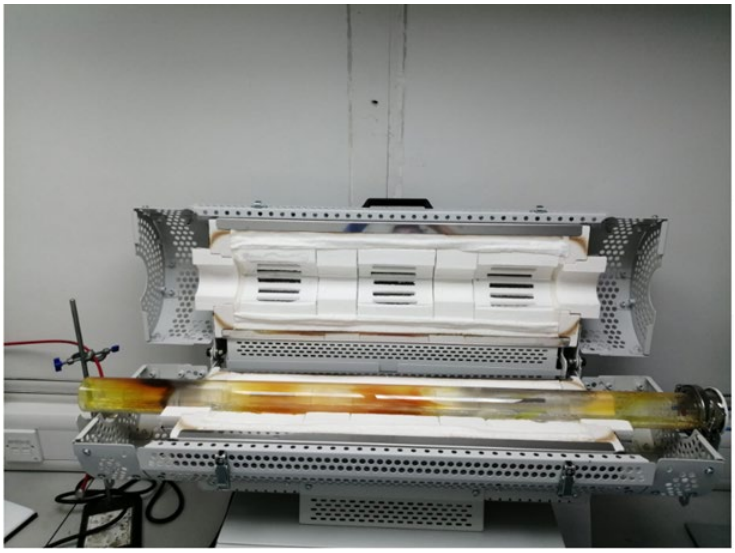

Figure 5.2 Image of the ZS-3G Carbolite tube furnace and a quartz tube.

5.3 Materials

Chemicals used in this study have been listed in Table 5.1

Table 5.1 Table 3.1: List of chemicals used in this study.

Chemicals	Supplier	Purity
Bismuth (III) bromide	Sigma-Aldrich	99.998%
Bismuth (III) iodide	Sigma-Aldrich	99%
N, N-Dimethylformamide (DMF)	Sigma-Aldrich	99.80%
Bismuth (III) nitrate pentahydrate	Fisher scientific	99.999%
Vanadyl acetylacetonate	Sigma-Aldrich	98%
Acetone	Fisher scientific	>95%
Isopropyl alcohol	Sigma-Aldrich	>95%
Hellmanex III solution	Hellma	-
Fluorine doped tin oxide coated glass slide (FTO)	Sigma-Aldrich	100%
Nitrogen Zero Grade	BOC Ltd	99.998%
Air Zero Grade	BOC Ltd	-

5.4 Methodology

5.4.1 Synthesis of $BIVO_4$ in two steps process

First, BiOBr/BiOI were deposited onto FTO substrates using an AACVD process. Depositions were carried out under air. $BiBr_3$/BiI_3 was dissolved in N, N-dimethylformamide (DMF). The resulting solution was stirred for 30 min to dissolve BiBr3/BiI3 and then atomised. Aerosol droplets were generated using a TSI Model 3076 Constant Output Atomizer and air as carrier gas. The TSI Model 3076 Constant Output Atomizer was used in the recirculation mode, and larger droplets and condensed precursors were recycled in the precursor solution bubbler. Different times, temperatures, concentrations and flow rates of precursor were carried out to study the impact of these variables in the deposition and characteristics of the final film. At the end of the deposition time, the substrates were left to cool down under the carrier gas until 100ºC. The ZS-3G Carbolite tube furnace is divided into three 15 mm heated zones with two 75 mm unheated zones barriers. Each heated zone has its temperature controller and thermocouple, so different configurations were used in the experiments to study the impact in the film deposition.

FTO substrates were cleaned by ultrasonication in a 2% aqueous Hellmanex III solution, deionised water, acetone, and isopropyl alcohol (each step for 10 min) dried with compressed air followed by an oxygen plasma treatment for 20 min to enhance surface energy and finally stored in deionised water. Different positions and configurations of the substrates in the tube were studied.

Secondly, BiOBr/BiOI were transformed into $BiVO_4$ using a process described by Tae Woo Kim and Kyoung-Shin Choi.[42] Briefly, 0.15-0.2 mL of a dimethyl sulfoxide (DMSO) solution containing 0.2 M vanadyl acetylacetonate ($VO(acac)_2$) was placed on the BiOI/BiOBr substrates. The substrates were annealed at 450 ºC with a ramping rate of 2 ºC/min for 2 h.

Finally, the excess of V_2O_5 present in the $BiOV_4$ was removed by soaking the substrates in 1 M NaOH solution with gentle stirring until all the V_2O_5 was eliminated. The final substrates were rinsed with deionised water, dried with compressed air and stored at room temperature.

5.4.2 Synthesis of $BIVO_4$ in one AACVD step process

Bismuth(III) nitrate pentahydrate and vanadyl acetylacetonate were dissolved in DMF. The resulting solution was stirred for 30 min to dissolve the solutes and then atomised. The droplets were generated using the same TSI Model 3076 Constant Output

Atomizer as the 2 steps process, and air or nitrogen as carrier gas was used. Different times, temperatures, concentrations and flow rates of precursor were carried out to study the impact of these variables in the deposition of the film. At the end of the deposition time, the substrates were left to cool down under the carrier gas until 100ºC. FTO was cleaned with the same process as the 2 steps process.

The V_2O_5 present in the $BiOV_4$ after the deposition was removed by soaking the substrates in 1 M NaOH solution with gentle stirring until all the V_2O_5 was eliminated. The final substrates were rinsed with deionised water, dried with compressed air and stored at room temperature.

5.4.3 Final experiments studied

The final experiments performed were as follows:

<u>BiOBr two-step process</u>

It was only studied under the conditions of 100 ºC in the first heater, 300 ºC in the second and third heater and 3 hours of deposition (BiOBr).

The transformation in $BiVO_4$ was carried out as explained in section 1.4.1.

<u>BiOI two-step process</u>

Different times of deposition were studied with 100ºC in the first heater, 300 ºC in the second and third heater: 3 hours (BiOI 3h), 5 hours (BiOI 5h) and 7 hours (BiOI 7h).

In addition, the influence of the temperature change in the process was also studied, for 5h of deposition a configuration of 100 ºC in the first heater, 350 ºC in the second and third heater ($BiVO_4$ from BiOI 5h 350 ºC) and a configuration of 100 ºC in the first heater, 400 ºC in the second and third heater (Component 400ºC) were studied. Meanwhile, for 7h of deposition, a configuration of 100 ºC in the first heater, 350 ºC in the second and third heater ($BiVO_4$ from BiOI 7h 350 ºC) was studied.

The transformation in $BiVO_4$ was carried out as explained in section 1.4.1.

In both cases (BiOI/BiOBr), FTO samples were placed in the second heater.

The deposition was not studied at a time of 7h and 400 ºC because at this temperature for the 5h process, a yellowish compound was formed instead of the BiOI (reddish). This yellowish compound is also present in the rest of the experiment, but it appeared in a residual form in the last FTO located in the tube. When the temperature was

increased to 350 ºC, the yellow part deposited increased in size in the last FTO, and at the temperature of 400 ºC, most of the deposition was of the yellow compound.

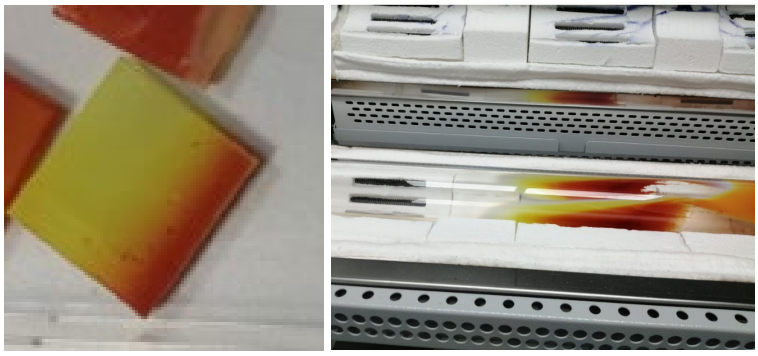

Figure 5.3 image of the yellow compound generated at 400 ºC and image of the tube after the experiment

$BiVO_4$ in one-step process

For the deposition of $BiVO_4$ in one step, a temperature of 400 ºc was used in the 3 heaters.

The deposition of the $BiVO_4$ in the FTO occurred between the last insulator and the last heater.

5.5 Security and flammability limits of the solution

AACVD involves atomising a precursor solution fine, sub-micrometre-sized aerosol droplets, which are delivered to a heated reaction zone. Although the process temperature is usually lower than in the CVD, it is crucial to avoid security problems due to the possible solution accumulation within the closed system. In general, if the carrier gas is an inert gas like nitrogen, the only issue to consider is air entrance from the outside through leaks in the connections. On the other hand, if the carrier gas is air, the limits of exposition of the mixture air-solution must be calculated to ensure the correct operation of the system. The solvent's autoignition temperature is another crucial factor since it marks the temperature limit of operating the process. However, it is essential to consider the percentage of solvent in the air that enters the tube furnace. It is generally shallow and allows this temperature to be increased as long as it is checked that there is no type of obstruction at the outlet system. Finally, check that the solutes and solvents used do not create more reactive mixtures or produce more dangerous by-products.

DMF was used as a unique solvent in all the experiments and the solutes used do not create dangerous mixtures with it. The autoignition temperature of DMF is 440ºc; this temperature can be considered as the limit temperature in the experiments.

The lower flammability temperature at 400ºC is 1.672%. The percentage of DMF in the air that enters per second for 3 litres per minute using TSI Model 3076 Constant Output Atomizer (maximum flow used in the experiments) is 0.00355%. The tube volume inside the furnace is 2.49 dm^3, so the atomizer would have to work for 7.20 h without any air outlet to create a flammability atmosphere.

5.6 Characterization

5.6.1 X-ray diffraction (XRD)

The composition and crystal equivalence information of the samples was determined by X-ray diffraction characterisation. The machine PANalytical X'Pert, incident irradiation beam (Cu Ka1, lambda = 1.5405980 A, and Cu Ka2, lambda = 1.5444260 A in ratio 1:0.5) operated at 40 kV and 20 mA current with a scan step size 0.0334225, range 10° to 80°.

5.6.2 UV Vis Spectroscopy

UV-VIS is a quantitative technique used to measure how much a chemical substance absorbs light. SHIMADZU UV-2600 measured the reflectance and absorbance in part of the ultraviolet and the entire adjacent visible regions of the electromagnetic spectrum.

5.6.3 Scanning electron microscope (SEM)

A scanning electron microscope (SEM) scans a focused electron beam over a surface to create an image. The electrons react with the sample, creating various signals that can be used to obtain information about the surface topography and composition. Zeiss Auriga Cross Beam microscope was used to obtain top-down and side-on images.

5.6.4 Thermogravimetric Analysis (TGA)

Thermogravimetric Analyzer TGA measures the amount and rate of weight change in a material, either as a function of increasing temperature or time, in a controlled atmosphere. Thermogravimetric analysis (TGA) was performed using TA Q500 TGA equipment for different solutes powders.

5.6.5 Raman spectroscopy

Raman spectroscopy was carried out on a system using a SENTERRA II. The laser beam was focused onto the sample using a 20x long distance objective with a 532nm laser, aperture 25x1000 um and resolution of 4 cm^{-1}.

5.6.6 PEC measurements

CompactStat. potentiostat (Ivium Technologies) was used in the PEC performance of photoanodes. Photocurrents were measured under simulated sunlight (AM 1.5G, 100 $mWcm^{-2}$) from a filtered 300 W xenon lamp source (Lot Quantum Design). Measurements were carried out in a three-electrode PEC cell with a quartz window, working electrode, Pt wire counter electrode, silver chloride Ag/AgCl as reference electrode, and 0.5 M Na_2SO_4 with a pH=6.5 as the electrolyte solution. Illumination was sent to the back of the FTO working electrode, and photocurrent-time curves were measured at an applied bias of 1.23 V vs the reversible hydrogen electrode (VRHE). The Ag/AgCl potentials were converted to RHE potentials using the Nernst equation:

$$E^{o}_{RHE} = E^{o}_{Ag/AgCl} + E_{Ag/AgCl} + 0.059 \qquad 5\text{-}1$$

5.7 Results and discussion

The influence of different parameters and configurations were studied for the AACVD process in the synthesis of BiOBr / BiOI and $BiVO_4$. The objective was to understand how these changes can affect the adhesion and deposition of the film onto the substrate and if it is possible to apply these results to processes that use similar precursors in the future.

5.7.1 Flow rates ranges and carrier gas

The carrier gas was air or nitrogen and the flow rates varied between 2 (20 psig) and 3 (37 psig) litres per minute (LPM). A flow meter was used in an experiment with only the carrier gas and without solvent to measure the flow rate. Depending on the solvent and the flow of the atomizer, the amount of precursor in the carrier gas that enters inside the tube changes; using DMF as the solvent with 2 LPM, the amount of solvent in the carrier gas is 0.00000135 L/s meanwhile with 3 LPM the amount of solvent is 0.00000178 L/s. The different inherent features of solvents, such as volatility or solubility with the precursor used, can alter the solution's delivery rates and mass-transport properties in the reaction system and, thus, modify the reaction pathways of chemical precursors in the gas phase. One of the disadvantages of the atomizer is the time required to produce a good film due to the low amount of solvent in the carrier gas. However, the droplets generated are tiny and controlling the type of deposition should be better.

Due to the pressure increase and the small hole at the tube entrance, the flow until the first heater is concentrated in the middle and push the air with the precursor in the top and the bottom to crash with the wall creating a recirculation zone and an

accumulation of precursor in the entrance. This accumulation produces a considerable loss of precursor in this zone.

Figure 5.4 Recirculation and accumulation zones in the entrance of the tube.

On the other hand, there is an accumulation of particles at the end of the tube since the flow must come out through a small hole, also creating a recirculation zone.

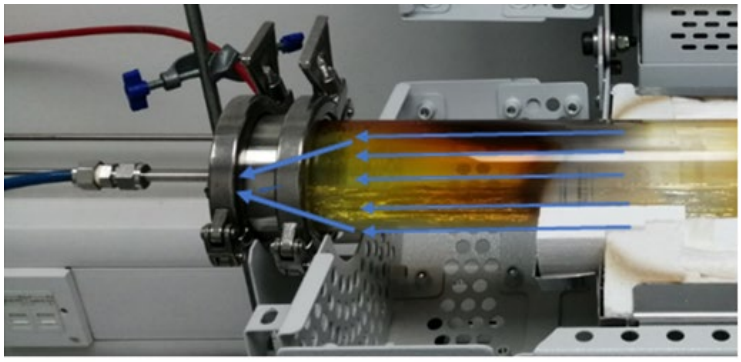

Figure 5.5 Accumulation zones at the entrance of the tube.

In Figure 5.5, an experiment with 500 ºC in the 3 heaters was carried out at higher temperatures. Higher temperatures increase the accumulation zones due to the higher evaporation rate of the precursor. The deposition is produced in the entrance, and the final of the tube and this deposition finish (entrance) or starts (end of the tube) in the insulation part (blue circles) and nothing was deposited in the middle. The deposition is produced in these zones because the insulation parts reduce the temperature and the precursor condensates; meanwhile, the temperature is too high to make a deposition in the middle of the tube. In addition, the fact that the entrance area is fully covered reinforces the hypothesis that there is recirculation in this area.

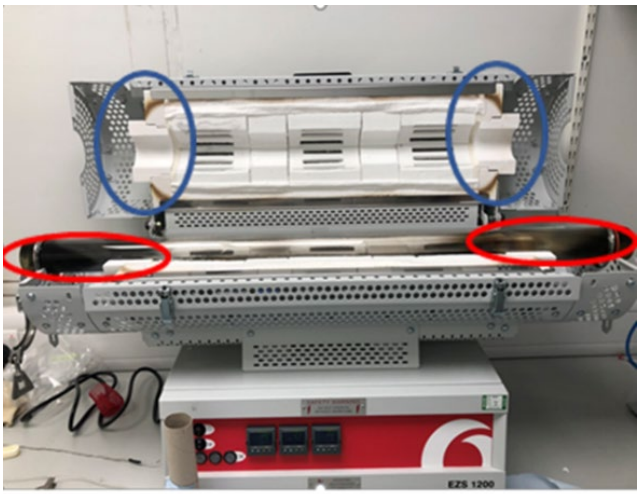

Figure 5.6 Accumulation zones with an experiment of 500 ºC.

5.7.2 Temperature

Temperature is one of the most critical parameters of the process. ZS-3G Carbolite tube furnace with 3 heaters separated with unheated zone barriers and a quartz tube were used in the experiments. Different configurations of temperature were studied in the process:

Homogeneous temperature: All the heaters work with the same temperature in this configuration. In this case, the deposition occurs mainly in the first FTO, which was generally in the area of the first insulator (between the first heater and the insulator), the top walls and at the end of the tube.

The deposition in this first zone may be highly influenced by the recirculation zone generated by the pressure inlet. The deposition in this zone could be mainly heterogeneous due to the cooling of the insulator zone.

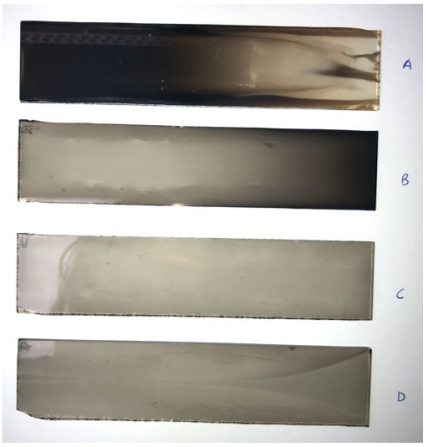

Figure 5.7 Comparative of the amount deposited in FTO with 500ºC in order of placement in the tube (A-D).

Temperature ramp: A ramped temperature was used along the tube to avoid the above situation and generate a more controlled deposition in the hot zone. A lower temperature was set in the first heater (generally 100ºC) compared with the other 2 heaters, and the deposition was mainly in the second heater. In Figure 5.8, It can be seen how the deposition is primarily in the second and third heater, while in the first heater, the tube is almost transparent.

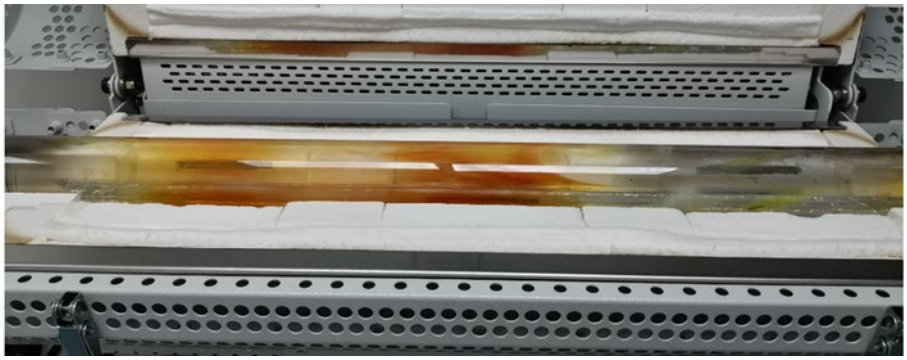

Figure 5.8 Deposition comparative of the 3 heaters.

The idea of this configuration was to create a heterogeneous deposition with better control and avoid the deposition of possible by-products that could be generated with other types of secondary reactions.

In the one-step synthesis process of $BiVO_4$, the deposition was produced between the last isolator and the last heater in both configurations; meanwhile, V_2O_4 was deposited in the normal position, the deposition was mainly in the second heater for the ramp temperature configuration and deposition in the first FTO which was generally in the area of the first insulator for the homogeneous configuration. The cause of this deposition can be the time necessary to produce $BiVO_4$ through secondary reactions. In the first part of the tube, the principal reactions produce V_2O_4, but along the tube, other types of reactions appear with the increase of the temperature of the carrier gas. The deposition of V_2O_4 is principally heterogeneous; meanwhile, the deposition of $BiVO_4$ is homogenous, producing a very bad adhesion with the FTO.

The deposition in the 2 configurations occurred mainly in the upper part of the tube; this could be because the contact between the insulation areas and the tube is worse, generating a layer of air that reduces the temperature creating a slight temperature gradient. On the other hand, this gradient should favour the deposition that occurs with endothermic reactions on FTO.

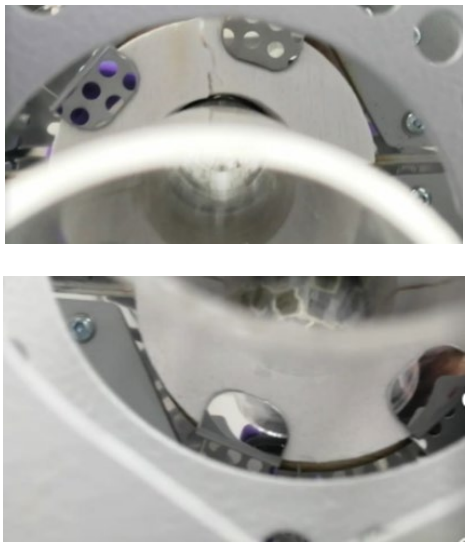

Figure 5.9 Comparison of the contact of the insulating part with the tube at the top and bottom.

5.7.3 Structures

Different structures to support the FTO were tested, but the difference was insignificant. The objectives were to reduce the distance between the flow of the gas and the FTO, improve the deposition on the FTO, and reduce the loss of precursor in the tube walls since the tube's length and diameter were too large for the process.

The standard structure was the tube with a metal structure of 3 bars closed with aluminium to support FTO. The connection between the FTO and the structure piece was not so good since there were small holes with no type of contact. In addition, a more significant gradient of temperature was created between the top and the bottom of the tube. Using a metal piece should favour the depositions that occur with endothermic reactions but negatively affect the deposition produced by exothermic reactions.

Figure 5.10 metal structure of 3 bars closed with aluminium to support FTO.

A rectangular metal structure was built to carry out experiments. It was a structure that reduced the space the air could flow with the precursor from the entrance to the last heater. However, after one experiment, one of the supports broke since the materials used to fabricate it and keep the structure inside the tube were made of a

fragile material that broke very easily. The result of the experiment was favourable since the deposition was improved.

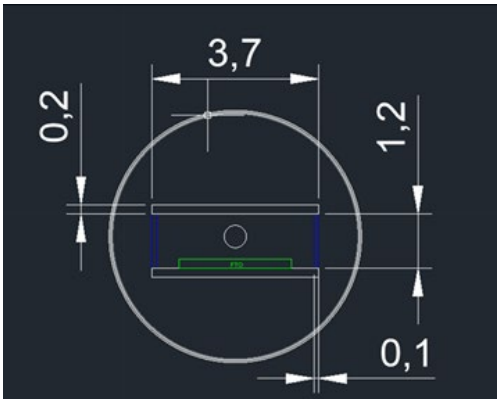

Figure 5.11 Dimensions of the rectangular structure created in Auto-Cad.

Another idea was to use another tube with a smaller diameter inside the big tube. The problem with this structure was controlling the temperature as the layer in the top of the small tube created a more significant temperature gradient. The experiments were better for the deposition of BiOBr, but for BiOI and $BiOV_4$, similar results were achieved concerning the standard tube with the metal structure. This configuration was used in most experiments to synthesise $BiVO_4$ in one step.

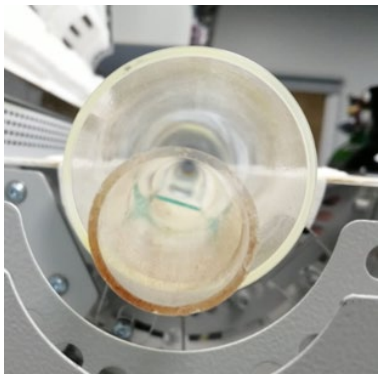

Figure 5.12 Structure with the two tubes, comparative of the diameters.

The final structure was another new metal piece with the length of the heaters with a flat top to perfectly support the FTO and the shape of the tube on the bottom. This configuration was used in the important experiments to synthesise BiOI in the two-step process. In this case, the temperature gradient is mainly concentrated in the heater producing a better deposition as the surface of the FTO is in complete contact with the metal piece.

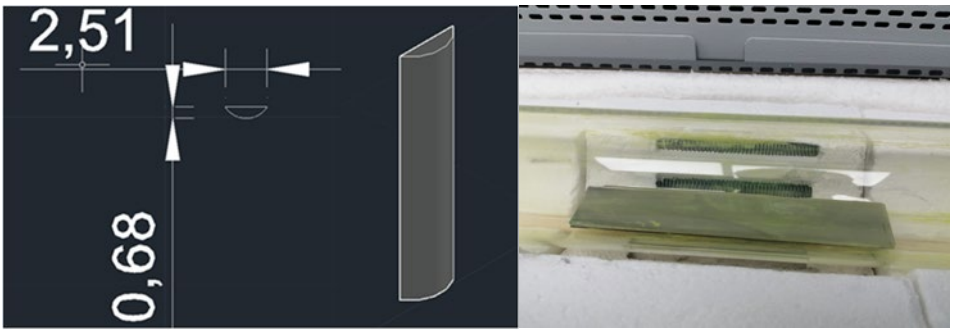

Figure 5.13 Dimensions of the last metal structure and the position in the tube.

5.7.4 Physical Characterisation

X-ray diffraction (XRD)

Different XRD analyses were made to compare the distribution:

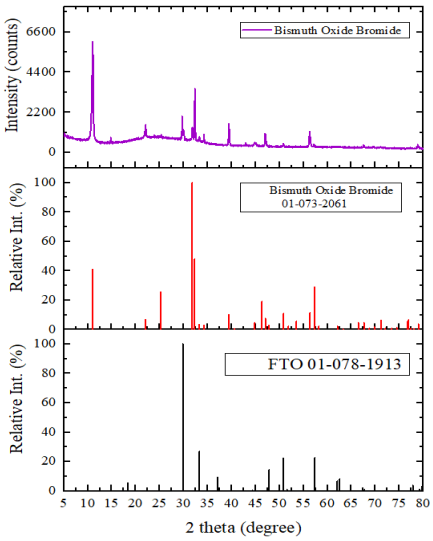

Figure 5.14 XRD patterns of standard FTO, standard bismuth oxide bromide and bismuth oxide bromide deposited.

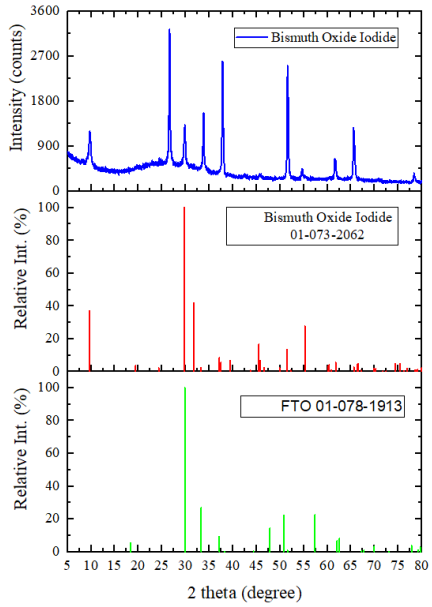

Figure 5.15 XRD patterns of standard FTO, standard bismuth oxide Iodide and bismuth oxide iodide deposited.

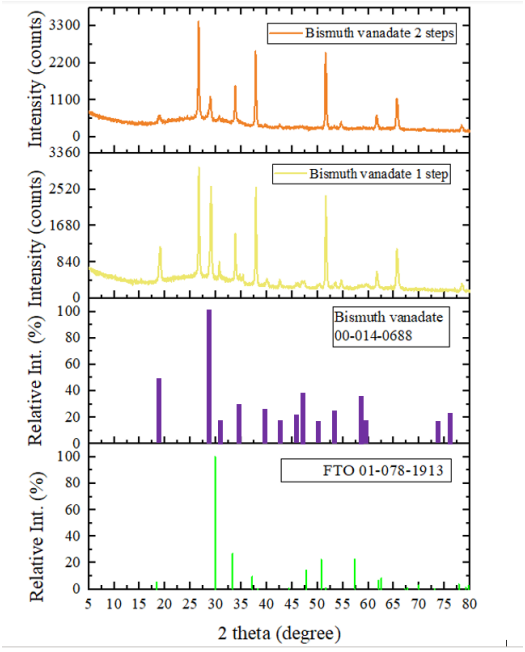

Figure 5.16 XRD patterns of standard FTO, standard bismuth vanadate and bismuth vanadate deposited in one-step and two-step processes.

The XRD patterns confirmed the presence of BiOI, BiOBr and $BiVO_4$ in the two-step process and the one-step process. BiOI and BiOBr were phased pure and crystallised in the tetragonal matlockite structure.

$BiVO_4$ patterns confirm the monoclinic scheelite. The peaks of $BiVO_4$ in the two-step process and the one-step process are very similar, ensuring that $BiVO_4$ could be generated in different ways.

However, a complete analysis of the changes generated under different conditions was not carried out since the XRD was only used to confirm the presence of the other compounds.

UV-Vis

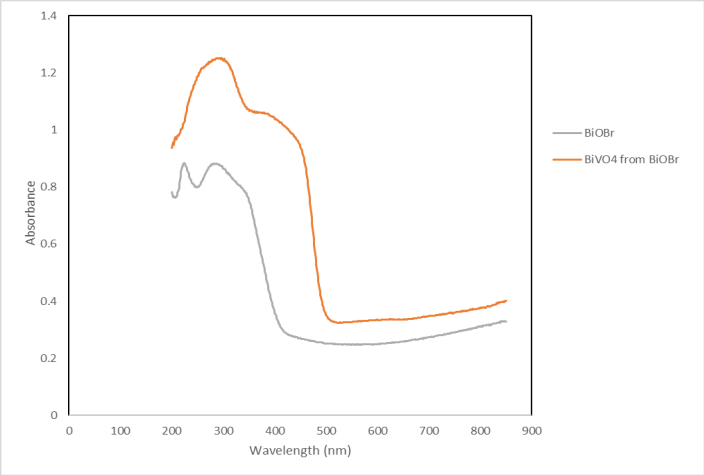

Figure 5.17 Absorbance of BiOBr and $BiVO_4$ from BiOBr.

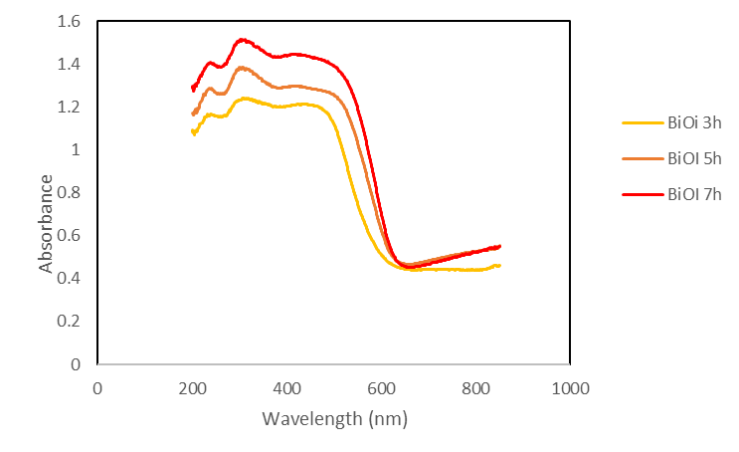

Figure 5.18 Absorbance of BiOI in different times.

The absorbance of BiOI at different times shows that the absorption edge increases when the time of deposition is longer. In addition, the absorption edge of all of the BiOI deposition at different times have an absorption edge with a bigger value than BiOBr.

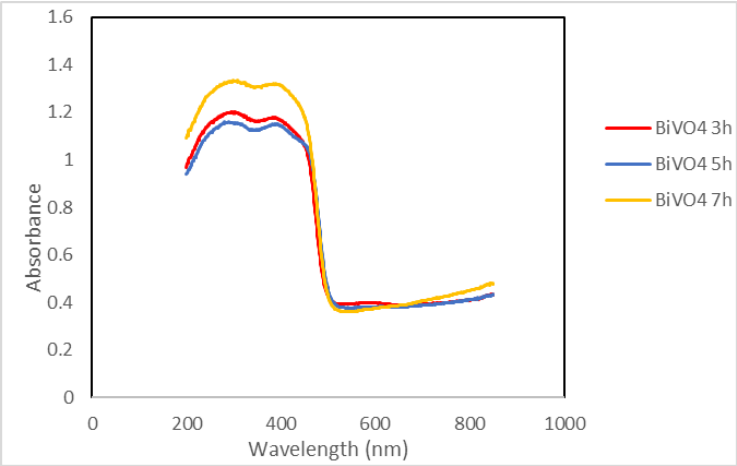

Figure 5.19 Absorbance of $BiVO_4$ from BiOI at different times.

However, when the BiOI/BiOBr is transformed into $BiVO_4$, the absorption edge is in the same position in all the cases. This could indicate that there is homogenisation after its transformation.

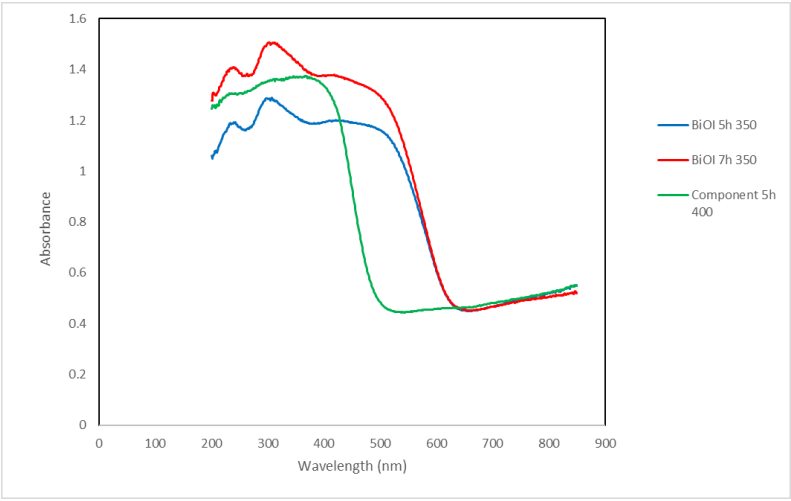

Figure 5.20 Absorbance of BiOI in different temperatures and the formation of the component at 400 ºC.

In the case of BiOI at different temperatures, the absorption edge is slightly displaced, so when the temperature increases, it could indicate that there is not much difference in the deposition in 5h or 7h. However, the component formed at 400 ºC presents a different absorption edge respect BiOI.

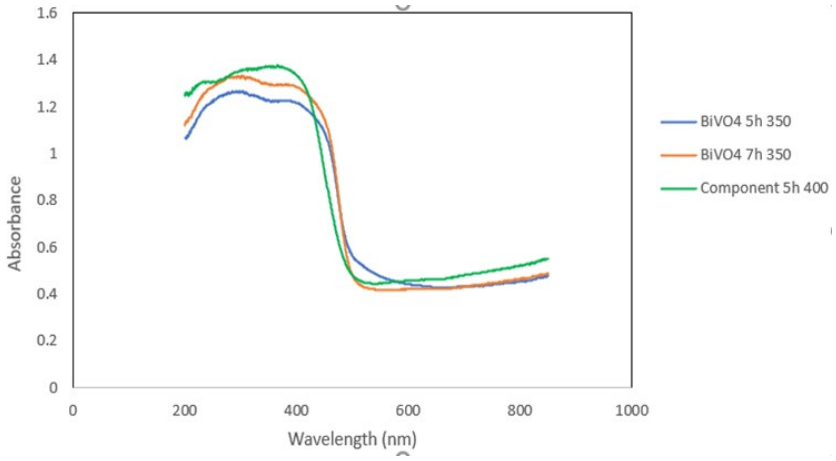

Figure 5.21 Absorbance of $BiVO_4$ from BiOI in different temperatures.

The compound formed at 400 ºC presents an absorption edge similar to the $BiVO_4$. Although it is slightly displaced to the left with respect to the other two $BiVO_4$ absorbance edges, it could indicate that it is $BiVO_4$, but It can also be another compound that could be interesting to study. The production of this compound is possible due to secondary reactions that take place at higher temperatures. Again, after transformation, the produced BIVO4 present the same absorption edge. This indicates that the second stage has a more significant impact on absorption

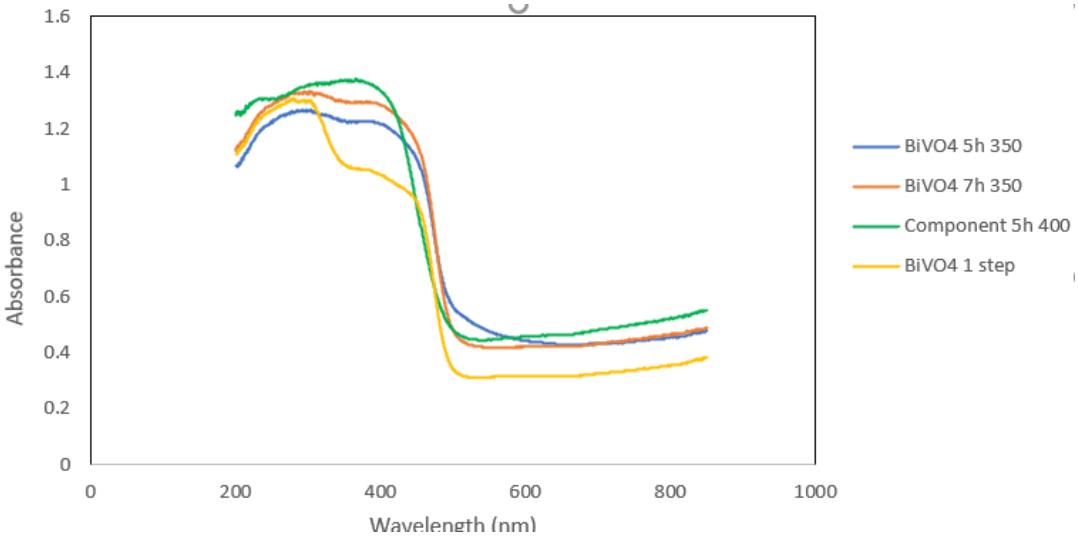

Figure 5.22 Absorbance of $BiVO_4$ of the one-step process compared with Figure 5.20.

In this case, the $BiVO_4$ produced in a one-step process presents a different absorption edge compared with the $BiVO_4$ made in a two-step process.

Scanning electron microscope (SEM)

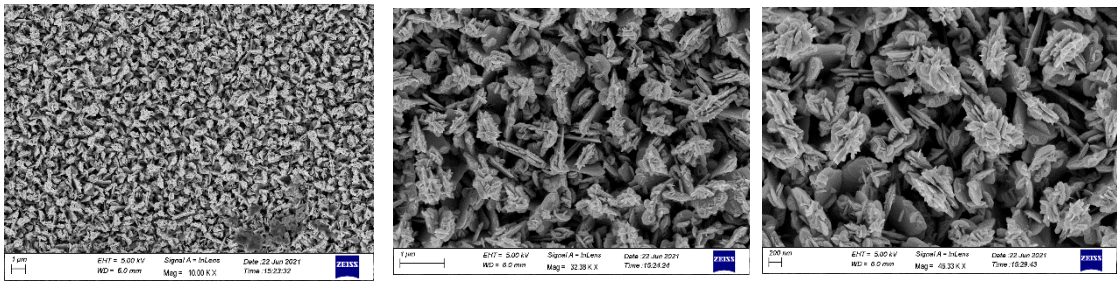

Figure 5.23 SEM micrographs at different magnifications of BiOBr.

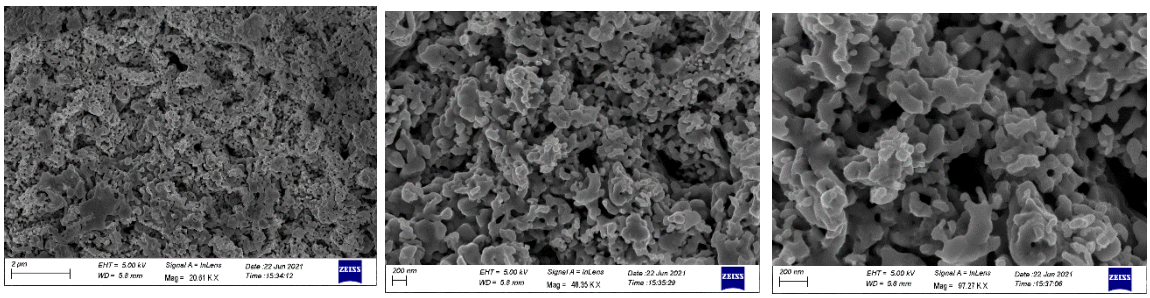

Figure 5.24 SEM micrographs at different magnifications of $BiVO_4$ from BiOBr.

The BiOBr sample consists of clusters of crystallites contributing to the particles resembling nanoflowers. The clusters appear to be composed of smaller crystallites. However, when transformed into $BiVO_4$, these structures lose shape and become more rounded. The structures leave a lot of gaps between them, creating porous, so it could be beneficial in the problem of electron recombination since there is an increase in the surface in contact with the electrolyte

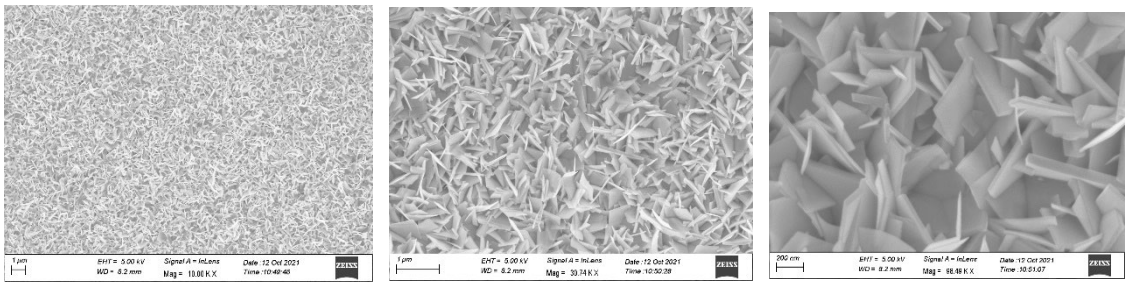

Figure 5.25 SEM micrographs at different magnifications of BIOI 3h.

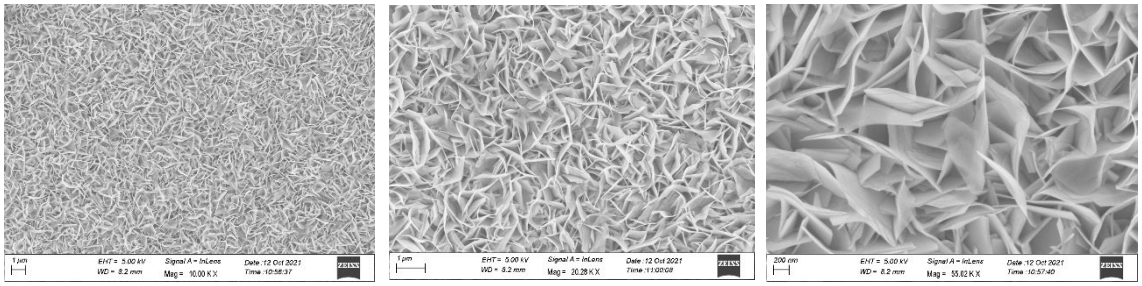

Figure 5.26 SEM micrographs at different magnifications of BIOI 5h.

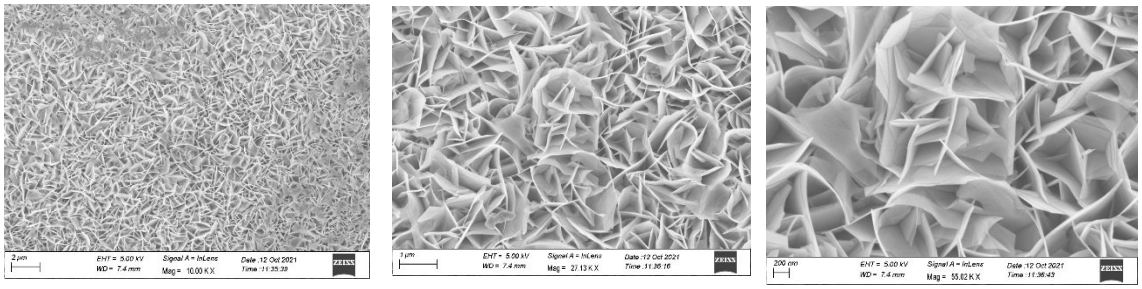

Figure 5.27 SEM micrographs at different magnifications of BIOI 7h

In the case of BiOI, the structure consists of a nanoplatelet morphology. As the deposition time increases, these structures become more extensive, but the width decreases with the time becoming almost flat by the 7h process. For the case of 3h, the structures are practically joined rectangles, while when the deposition time is increased, they unite more and more until they form chains and there is no defined shape.

Both for the case of BiOBr and BiOI, the electronic properties of these materials are anisotropic, and this faceted growth may help charge carrier mobility along with certain facets.

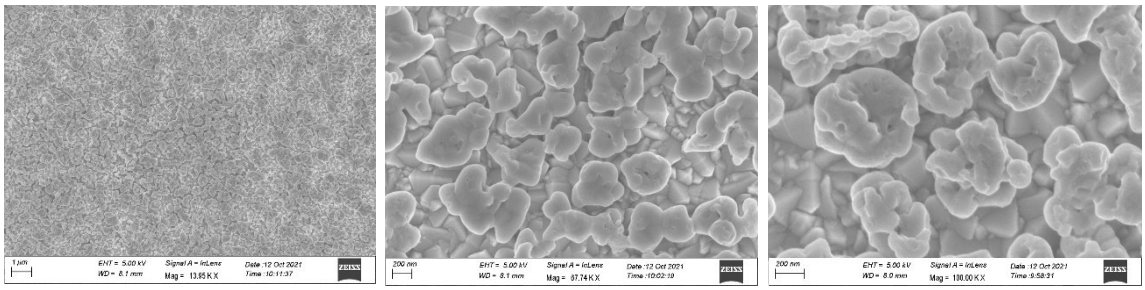

Figure 5.28 SEM micrographs at different magnifications of $BiVO_4$ from BiOI 3h.

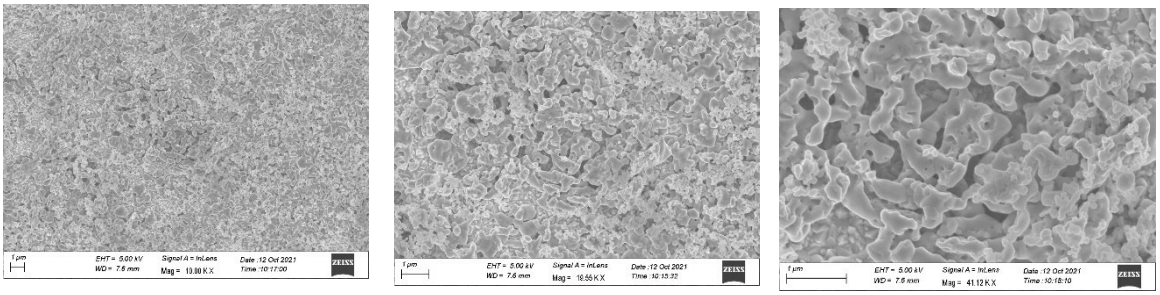

Figure 5.29 SEM micrographs at different magnifications of $BiVO_4$ from BiOI 5h.

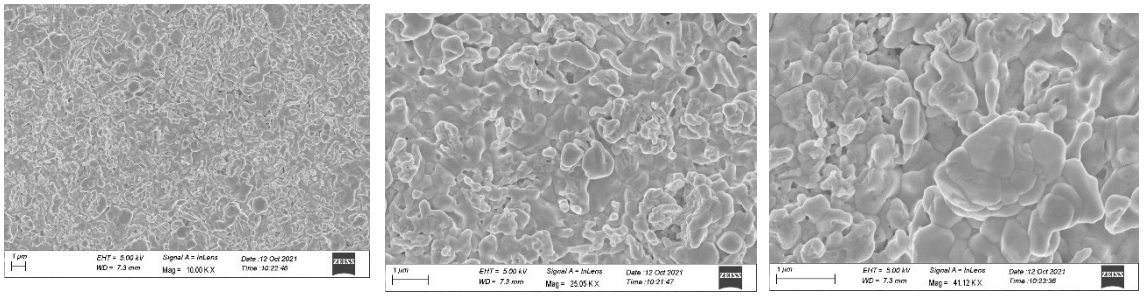

Figure 5.30 SEM micrographs at different magnifications of $BiVO_4$ from BiOI 7h.

When it becomes $BiVO_4$, it can be seen that for the 3h deposition, there is still some separation in the rounded structures that are formed. However, as the deposition time increases, the forms become less and less appreciated. In the 5h deposition, some separation between the structures is still appreciated. In comparison, in the 7h deposition, the structures form a more homogeneous mass with almost no gaps and no porous.

The morphology of the structures formed is a fundamental factor in improving semiconductors' performance for PEC services. $BiVO_4$ suffers from rapid photocarrier recombination as a result of short electron diffusion length (with only 10 nm) that affects its apparent quantum efficiency directly; photocurrent stability is not very good due to form a dissolution of V_{5+} ions in the solution and reactions in the surface of the photoelectrode such as O_2 and H_2O_2 that act as centres where there is recombination and is a material that suffers for a slow hole transfer kinetic producing a poor surface water oxidation. Some studies reveal that increasing the contact surface could improve electron recombination and perform better. In this sense, the homogenisation of the structures with increasing time could be a negative factor because the number of pores is drastically reduced.

Porosity gives the films a large effective surface area and an increased electrode/electrolyte interfacial area, reducing electron-hole recombination as the

photogenerated hole travels through less material before being collected at the electrode/electrolyte interface.

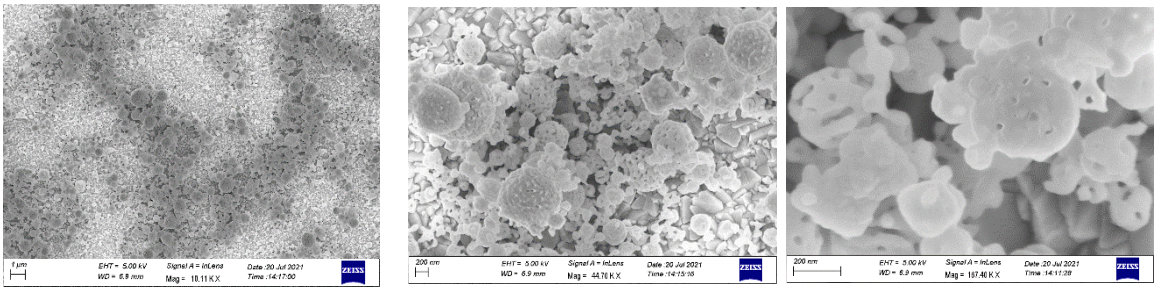

Figure 5.31 SEM micrographs at different magnifications of $BiVO_4$ one-step process.

In the one-step process, it is observed that there are areas of the surface of the FTO where there is no $BiVO_4$ deposited. In addition, sphere-shaped structures are formed, but there is no good contact with each other or with the FTO. This is in accordance with the idea that its deposition was through homogeneous reactions, and the adhesion is due to this type of reaction, so it is not an adequate deposition.

Thermogravimetric Analysis (TGA)

The thermogravimetric analysis of $BiBr_3$ BiI_3 and the solution of the precursor for the one-step process were studied to see the effect in experiments:

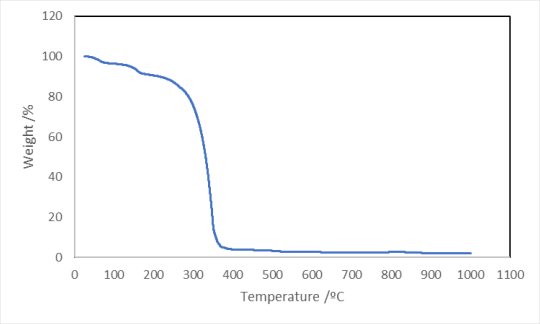

Figure 5.32 Thermogravimetric analysis (TGA) in Air of $BiBr_3$

The $BiBr_3$ has a decomposition temperature between 300 ºC and 400 ºC. Therefore, a higher temperature could favour the decomposition and deposition of a greater quantity of BiOBr. However, secondary reactions could affect the primary process in this range. There is a small decomposition zone between 25ºc and 300ºC, the temperature range where BiOBr deposition occurs in the experiments.

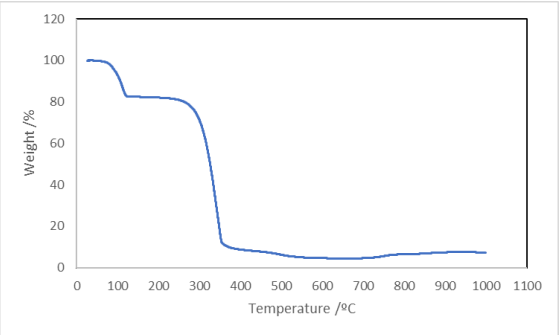

Figure 5.33 Thermogravimetric analysis (TGA) in Air of BiI_3

In this case for BiI_3, there are two quite different decomposition zones. This could explain why up to 350 ºC, the majority position was BiOI since up to 300 ºC, the first decomposition curve is found. It should be clarified that even if the temperature of the furnace was 300 ºC, the temperature of the air with the precursor that enters does not acquire it instantaneously but rather heat up as it advances through the tube. The second decomposition zone is also between 300 ºC and 400 ºC. This could explain why when a temperature of 400 ºC was used, practically no BiI_3 was found, but a yellow compound was formed that could be $BiVO_4$.

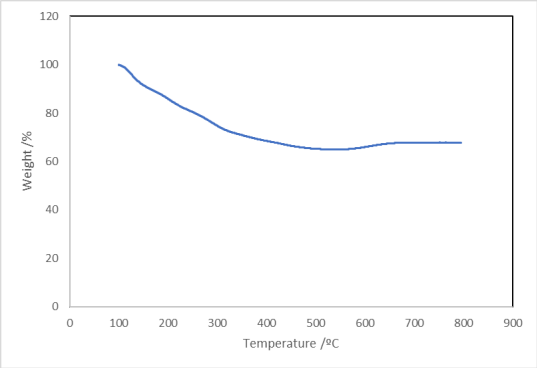

Figure 5.34 Thermogravimetric analysis (TGA) in nitrogen of the solution with DMF used in the one-step process

For the one-step process, the dissolution of DMF was studied together with the solutes, Bismuth (III) nitrate pentahydrate and Vanadyl acetylacetonate from 100 ºC with nitrogen. The result is not explanatory since differentiated areas are not seen, but a decomposition curve is up to almost 500 ºC and then another with a lower slope. 500 ºC could mark the location from which $BiVO_4$ could be forming.

Raman spectroscopy

Different Raman spectroscopies were made to compare the data with the other analysis:

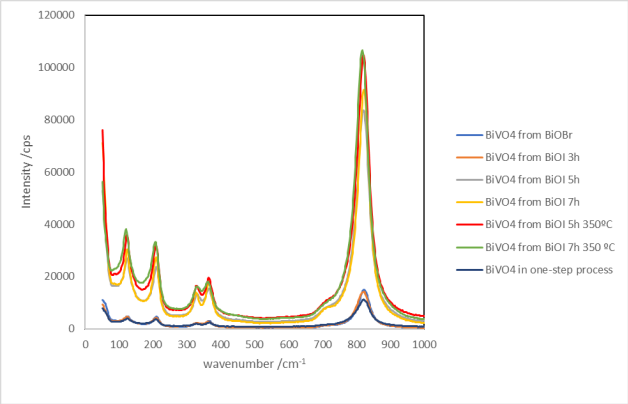

Figure 5.35 Raman spectroscopy of all $BiVO_4$ synthesized.

All $BiVO_4$, both in the two-step process and in the one-step process, show the peaks in the same positions. For the case of the one-step process, it is the one with the lowest intensity of all the $BiVO_4$. This could reinforce the theory that the adhesion with the FTO was bad. However, in the two-step process, the intensity of the peaks increases when the deposition time is more significant and increases when the operating temperature is bigger. The Raman spectrum shown in Figure 5.35 further confirms the formation of monoclinic scheelite $BiVO_4$. The most substantial peak at 827 cm^{-1} corresponds to antisymmetric stretching modes of the VO4 tetrahedra, while the shoulder peak at 718 cm-1 is attributed to the same symmetric stretching modes. The peaks at 366 and 326 cm^{-1} are due to the bending modes of the VO4 tetrahedra, and the peaks at 211 and 129 cm^{-1} correspond to the vibration of the crystal lattice (external modes).

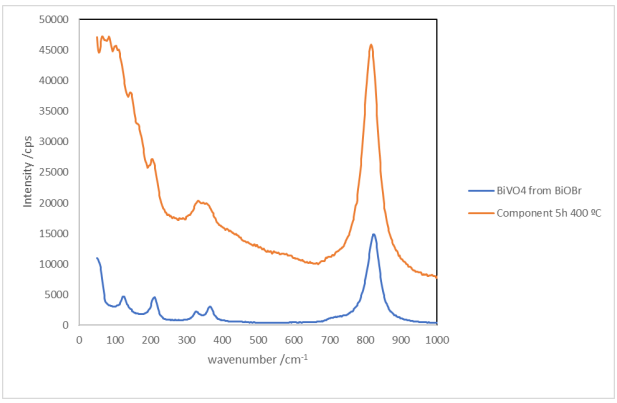

Figure 5.36 Comparative between the component deposited at 400 ºC 5h and $BiVO_4$ from BiOBr.

The component deposited at 400 ºC shows peaks similar to the rest of $BiVO_4$ but with other stranger peaks. The most substantial peak at 827 cm^{-1} is the peak that also appears and is differentiated. The peaks at 366 and 326 cm^{-1} can be appreciated but differently. The peak at 211 cm^{-1} can also be appreciated.

Looking at the results of this analysis, it could not be concluded that it is $BiVO_4$ since it seems to present other compounds. However, similar peaks could indicate that the one-step process using higher temperature with BiOI or BiOBr in DMF could be possible.

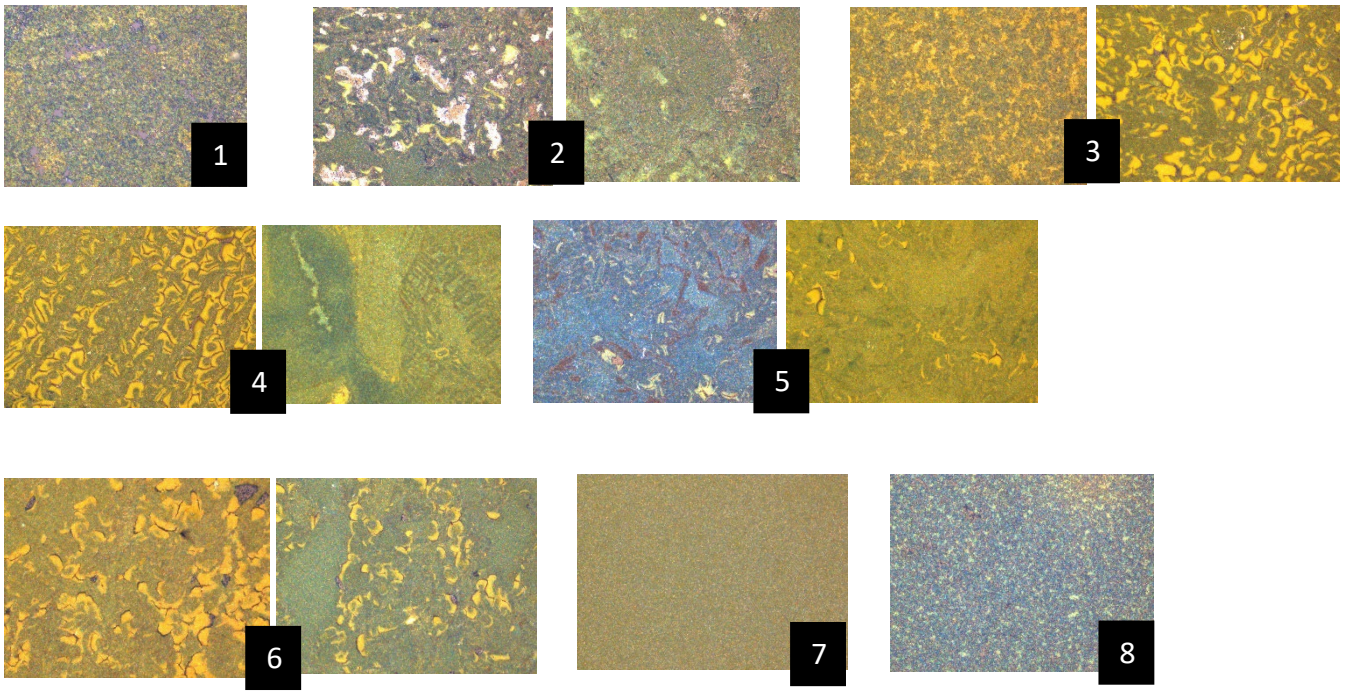

Figure 5.37 Raman spectroscopy images of all $BiVO_4$ synthesized. From BiOBr (1), from BiOI 3h (2), From BiOI 5h (3), from BiOI 7h (4), from BiOI 5h 350 ºC (5), from BiOI 7h 350 ºC (6), $BiVO_4$ from one-step process (7) and component 5h 400ºC (8).

The images show differences between the different experiments and the experiments performed at the exact times and temperatures. The difference between samples of the same experiments could be because, inside the tube, the deposition may change depending on the position due to the increasing temperature, so small different formations appear depending on the position. However, these differences should not affect much; finding the best place in the tube for the deposition could improve the results.

For the case of the one-step process and the compound produced at 400 ºC, the films are homogeneous.

5.7.5 PEC measurements

Measurements were carried out in a three-electrode PEC cell with a quartz window, working electrode, Pt wire counter electrode, silver chloride Ag/AgCl as reference electrode, and 0.5 M Na_2SO_4 with a pH=6.5 as the electrolyte solution. Illumination was sent to the back of the FTO working electrode, and photocurrent-time curves were measured at an applied bias of 1.23 V vs the reversible hydrogen electrode (VRHE).

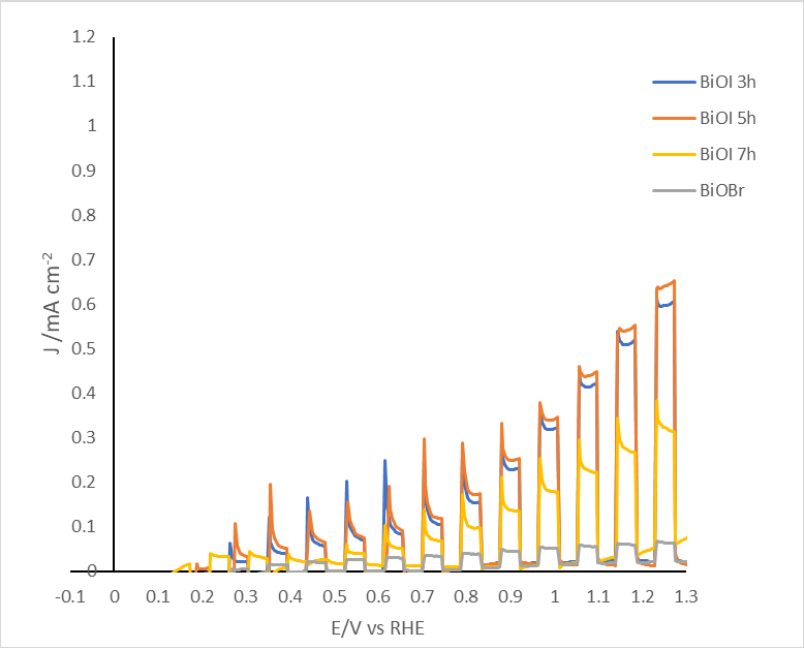

Figure 5.38 Photocurrent potential curves of BiOI at different times and BiOBr.

The Photocurrent potential curve for the deposition of BiOI time of 5h is the one with the highest value (0.7 mA cm^{-2} at 1.23V vs RHE). The lowest value for the deposition of BiOI at different times is the deposition of 7h. This could be due to the morphology change; as explained in the previous section, as the deposition time increases, these structures become more extensive, but the width decreases with time becoming almost flat by the 7h process.

For the deposition of BiOBr, the low value obtained compared to the deposition of BiOI is curious since they are similar materials that should have similar values.

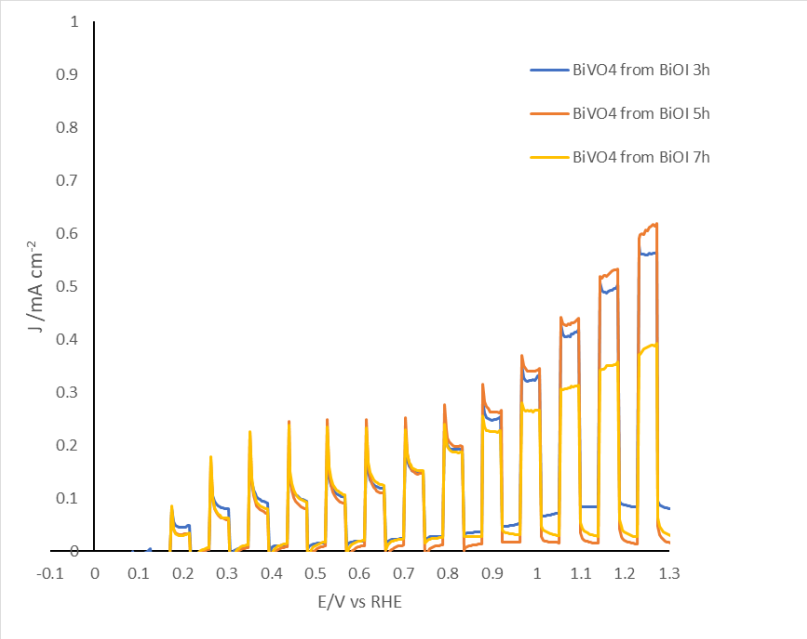

Figure 5.39 Photocurrent potential curves of $BiVO_4$ from BiOI at different times.

The values of Photocurrent potential for $BiVO_4$ after the transformation at different times, in general, have lower values than BiOI. However, the 5h deposition still has the highest value (0.6 mA cm^{-2} at 1.23V vs RHE), while the 7 h deposition shows the worst results. It is curious to observe that the values obtained for $BiVO_4$ after its transformation are lower than those obtained for BiOI. The transformation into $BiVO_4$ may modify the morphology generated during AACVD deposition of BiOI. Therefore, single-step deposition using AACVD could improve the results obtained by having better control of morphology.

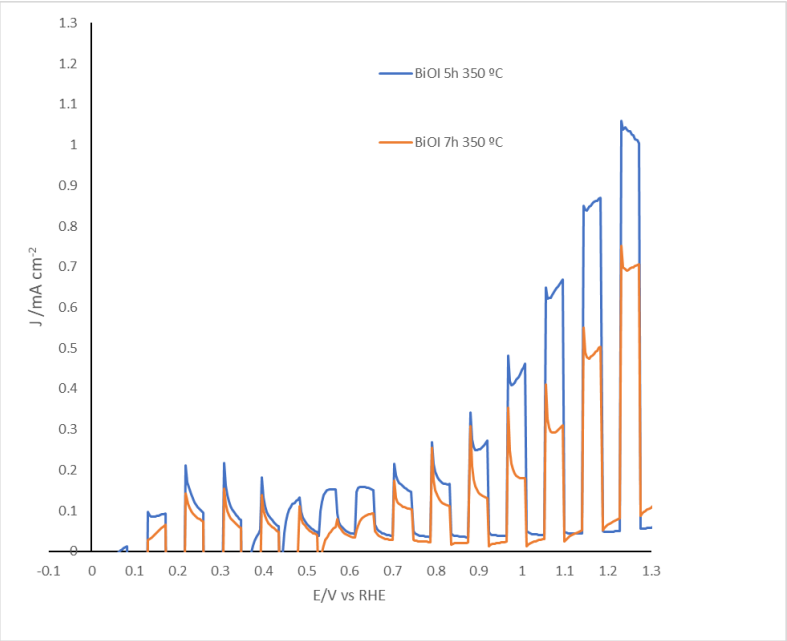

Figure 5.40 Photocurrent potential curves of BiOI at different temperatures.

The photocurrent potential curves of BiOI at different temperatures obtained show better results being the value of the deposition of 5h and 350 ºC the highest obtained from all samples tested (1.1 mA cm^{-2} at 1.23V vs RHE). This indicates that the increase in temperature positively influences the improvement of the results.

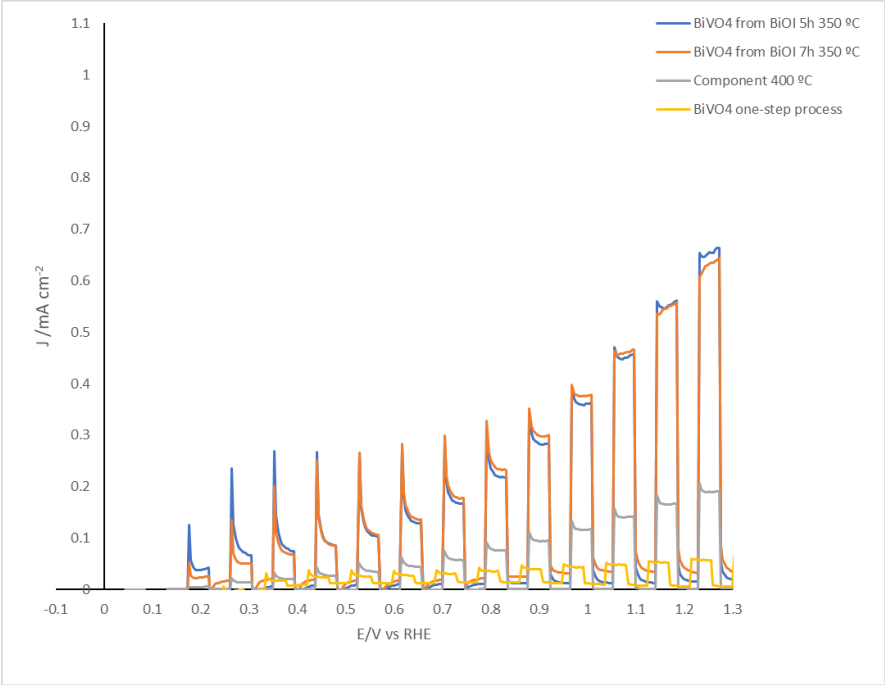

Figure 5.41 Photocurrent potential curves of $BiVO_4$ from BiOI at different times, component at 400 ºC and $BiVO_4$ in a one-step process.

Again, the values obtained after transformation into $BiVO_4$ are lower than for the deposition of BiOI at different temperatures. However, there is a slight improvement

compared to the data in Figure 5.39 photocurrent potential curves of $BiVO_4$ from BiOI at different times. Therefore, it reinforces the hypothesis that increasing the temperature improves the results obtained.

Although the values obtained for the component deposition at 400 ºC are low, it is a material that presents photocatalytic activity. A complete study of the material in question and the improvement of the conditions in its deposition could considerably improve the values obtained in this study.

Due to the bad adhesion between the FTO and the $BiVO_4$ deposited in the one-step process, the values obtained from photocurrent potential curves are too low to be considered.

Figure 5.42 Degradation of the samples of BiOI after PEC analysis.

Something to consider is the stability of the BiOI samples in all the pec analyses since they rapidly degraded, forming a black film on the part in contact with the electrolyte. This may negatively influence the results obtained as it is likely that better results would be obtained if the BiOI samples were more stable.

6 Conclusions

This work demonstrated the production of $BiVO_4$, BiOI and BIOBr for photoelectrochemical devices. In addition, a compound (probably $BiVO_4$) was generated at higher temperatures; it is a compound with a photocatalytic activity that could be investigated in more detail in the future. These photoanodes were grown by a two-step process or one-step process being the AACVD the primary process. Structures with different morphologies and characteristics were obtained.

Secondly, a study of the impact of different parameters in the deposition on FTO in AACVD processes was carried out. Factors such as flow rate and temperature

significantly impact the process. Its effects were studied by modifying its values to improve the experiments.

SEM micrographs showed nanoplatelet morphology for BiOI, nanoflower like particles were observed for the BiOBr film. However, when transformed into $BiVO_4$, these structures lose shape and become more rounded. In the one-step process, sphere-shaped structures are formed, but there is no good contact with each other or with the FTO.

In the one-step synthesis process of $BiVO_4$, in the first part of the tube, the principal reactions produce V_2O_4, but along the tube, other types of reactions appear with the increase of the temperature of the carrier gas. The deposition of V_2O_4 is principally heterogeneous; meanwhile, the deposition of $BiVO_4$ is homogenous, producing a very bad adhesion with the FTO.

In the Raman spectroscopy, all $BiVO_4$, both in the two-step process and one-step process, show the peaks in the same positions. The most substantial peak at 827 cm^{-1} corresponds to antisymmetric stretching modes of the VO4 tetrahedra, while the shoulder peak at 718 cm^{-1} is attributed to the same symmetric stretching modes. The peaks at 366 and 326 cm^{-1} are due to the bending modes of the VO_4 tetrahedra, and the peaks at 211 and 129 cm^{-1} correspond to the vibration of the crystal lattice (external modes). The component deposited at 400 ºC shows peaks similar to the rest of $BiVO_4$ but with other stranger peaks. In addition, the images of the Raman spectroscopy show differences between the different experiments and the experiments performed at the exact times and temperatures.

Photoelectrochemical measurements revealed that the best value was BiOI deposited for 5 hours and 350 ºC (1.1 mA cm^{-2} at 1.23V vs RHE). Although the initial objective was to obtain $BiVO_4$ as photoanodes, both in the two-step process and in the one-step process, lower values were obtained with respect to the BiOI deposition. In the two-step process, when it was transformed into $BiVO_4$, the maximum value reached in the BiOI before transformation into $BiVO_4$, was reduced being the best value the deposition for 5h and 350 ºC (0.7 mA cm^{-2} at 1.23V vs RHE), while in the one-step process, poor adhesion with the FTO produced very low values. However, BiOI rapidly degraded, forming a black film on the part in contact with the electrolyte.

7 BIBLIOGRAPHY

UNITED NATIONS. Sustainable Development Goals Report,2020.

ACS chemistry for life. 12 Principles of Green Chemistry, 2021.

BP, BP Statistical Review of World Energy, 2020.

International Energy Agency, Global Energy Status Report, 2020.

Royal Society of Chemistry, Solar Fuels and Artificial Photosynthesis, 2012.

Furat Dawood, Martin Anda, G.M. Shafiullah, Hydrogen production for energy: An overview, International Journal of Hydrogen Energy, 2020, vol. 45, Issue 7, pp. 3847-3869.

El-Shafie, M., Kambara, S. and Hayakawa, Y., Hydrogen Production Technologies Overview. Journal of Power and Energy Engineering, 2019 vol. 7, pp. 107-154.

R. J. Detz, J. N. H. Reek and B. C. C. Van Der Zwaan, Energy Environ. Sci., 2018, 11, 1653–1669.

B. A. Pinaud, J. D. Benck, L. C. Seitz, A. J. Forman, Z. Chen, T. G. Deutsch, B. D. James, K. N. Baum, G. N. Baum, S. Ardo, H. Wang, E. Miller and T. F. Jaramillo, Energy Environ. Sci., 2013, 6, 1983–2002.

A. Fujishima and K. Honda, Nature, 1972, 238, 37–38.

S. Giménez and J. Bisquert, Photoelectrochemical Solar Fuel Production: From Basic Principles to Advanced Devices, Springer International Publishing, 2016.

T Bak, J Nowotny, M Rekas, C.C Sorrell, Photo-electrochemical hydrogen generation from water using solar energy. Materials-related aspects, International Journal of Hydrogen Energy, Volume 27, Issue 10, 2002, Pages 991-1022, ISSN 0360-3199.

R. Van De Krol and M. Grätzel, Photoelectrochemical Hydrogen Production, Springer US, 2012.

H. Ahmad, S. K. Kamarudin, L. J. Minggu and M. Kassim, Renew. Sustain. Energy Rev., 2015, 43, 599–610.

S. Zhu and D. Wang, Adv. Energy Mater., 2017, 7, 1700841.

C. Jiang, S. J. A. Moniz, A. Wang, T. Zhang and J. Tang, Chem. Soc. Rev., 2017, 46, 4645–4660.

M. Grätzel, Nature, 2001, 414, 338–344.

K. Maeda and K. Domen, J. Phys. Chem. C, 2007, 111, 7851–7861.

H.-J. Lewerenz and L. Peter, Eds., Photoelectrochemical Water Splitting: Materials, Processes and Architectures, The Royal Society of Chemistry, 2014.

Z. Chen, H. N. Dinh and E. Miller, Photoelectrochemical water splitting: standards, experimental methods, and protocols, Springer, New York, 2013.

A. G. Tamirat, J. Rick, A. A. Dubale, W.-N. Su and B.-J.

Hwang, Nanoscale Horiz., 2016, 1, 243–267.

J. Li and N. Wu, Catal. Sci. Technol., 2015, 5, 1360–1384.

A. Kudo, K. Ueda, H. Kato and I. Mikami, Catal. Letters, 1998, 53, 229–230.

S. J. A. Moniz, S. A. Shevlin, D. J. Martin, Z.-X. Guo and J. Tang, Energy Environ. Sci., 2015, 8, 731–759.

Rayees Ahmad Rather, Akansha Mehta, Youming Lu, Matjaz Valant, Ming-Fang, Wenjun Liu, Influence of exposed facets, morphology and hetero-interfaces of BiVO4 on photocatalytic water oxidation: A review, International Journal of Hydrogen Energy, Volume 46, Issue 42, 2021, Pages 21866-21888, ISSN 0360-3199.

Y. Park, K. J. McDonald and K.-S. Choi, Chem. Soc. Rev., 2013, 42, 2321–2337.

Trinh, D.T.T., Khanitchaidecha, W., Channei, D. et al. Synthesis, characterization, and environmental applications of bismuth vanadate. Res Chem Intermed 45, 5217–5259 (2019).

Aron Walsh, Yanfa Yan, Muhammad N. Huda, Mowafak M. Al-Jassim, and Su-Huai Wei Chemistry of Materials 2009 21 (3), 547-551.

Kudo, A.; Omori, K.; Kato, H. A Novel Aqueous Process for Preparation of Crystal Form-Controlled and Highly Crystalline BiVO4 Powder from Layered Vanadates at Room Temperature and Its Photocatalytic and Photophysical Properties. J. Am. Chem. Soc. 1999, 121, 11459−11467.

Z. Zhao, Z. Li and Z. Zou, Phys. Chem. Chem. Phys., 2011, 13, 4746–4753.

D.J. Payne, M.D.M. Robinson, R.G. Egdell, A. Walsh, J. McNulty, K.E. Smith, et al., Appl. Phys. Lett. 98 (2011), 212110.

Carlsson J-O, Martin PM. Chemical vapour deposition. Handbook of Deposition Technologies for Films and Coatings (Third Edition): Elsevier; 2010. p. 314–63.

K. L. Choy, Prog. Mater. Sci., 2003, 48, 57–170.

P. Marchand, I. A. Hassan, I. P. Parkin and C. J. Carmalt, Dalt. Trans., 2013, 42, 9406–9422.

A. C. Jones and M. L. Hitchman, Chemical Vapour Deposition: Precursors, Processes and Applications, The Royal Society of Chemistry, 2009.

M. D. Allendorf and A. M. B. van Mol, Precursor Chem. Adv. Mater., 2005, 9, 1–48.

Pierson HO. Handbook of chemical vapor deposition. Park Ridge (NJ): Noyes; 1992.

Dobkin DM, Zuraw MK. Principles of chemical vapourdeposition. Dordrecht, The Netherlands: Kluwer AcademicPress; 2003.

A. C. Jones and M. L. Hitchman, Chemical Vapour Deposition: Precursors, Processes and Applications, The Royal Society of Chemistry, 2009.

X. Hou and K.-L. Choy, Chem. Vap. Depos., 2006, 12, 583–596.

T. W. Kim and K.-S. Choi, Science, 2014, 343, 990–994

Salvador Eslava, PhD
Senior Lecturer (Assoc. Prof.)
Department of Chemical Engineering
Imperial College London
London, SW7 2AZ, United Kingdom
Phone: +44(0)20 7594 8977
Email: s.eslava@imperial.ac.uk

Imperial College London

London, 9/1/2022

To Whom It May Concern,

I, Salvador Eslava, hereby declare that the thesis titled

Bismuth vanadate, bismuth oxyiodide and bismuth oxybromide thin films growth via Aerosol-Assisted CVD as the main process and their photoelectrochemical properties

reports the research carried out and written by Javier Vicente Matas under my supervision at Imperial College of London.

Dr Salvador Eslava
Senior Lecturer (Assoc. Prof.) in Chemical Engineering and EPSRC Early Career Fellow

Salvador Eslava

Digitally signed by Salvador Eslava
Date: 2022.01.09 13:21:45 Z